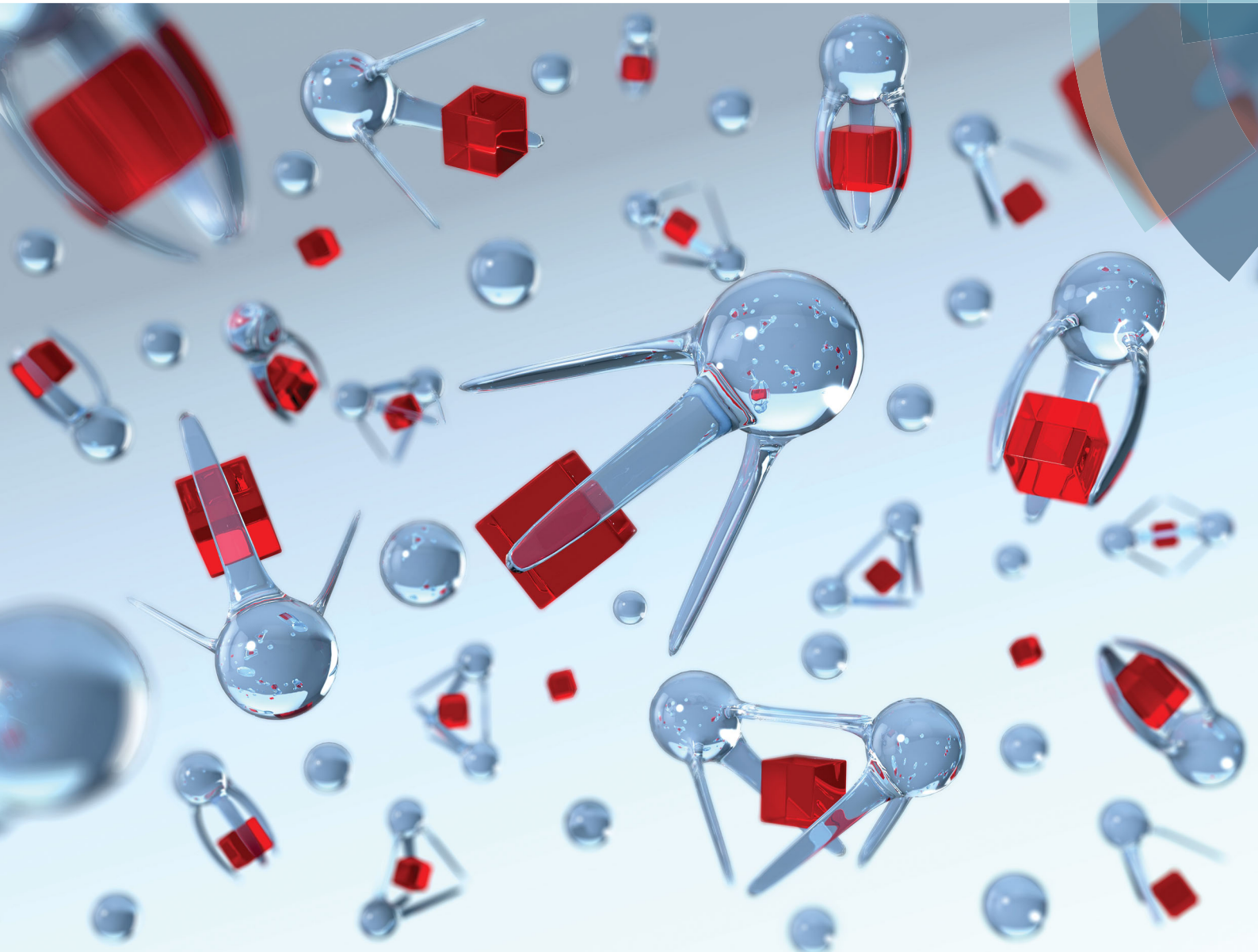


PCCP

Physical Chemistry Chemical Physics

rsc.li/pccp



ISSN 1463-9076



ROYAL SOCIETY
OF CHEMISTRY

PERSPECTIVE

Julius Koettgen, Manfred Martin *et al.*

Understanding the ionic conductivity maximum in doped ceria: trapping and blocking



Cite this: *Phys. Chem. Chem. Phys.*,
2018, 20, 14291

Understanding the ionic conductivity maximum in doped ceria: trapping and blocking†

Julius Koettgen,^{id}*^a Steffen Grieshammer,^{id}^{ab} Philipp Hein,^{id}^a
Benjamin O. H. Grope,^a Masanobu Nakayama^{id}^{cd} and Manfred Martin^{id}*^{abef}

Materials with high oxygen ion conductivity and low electronic conductivity are required for electrolytes in solid oxide fuel cells (SOFC) and high-temperature electrolysis (SOEC). A potential candidate for the electrolytes, which separate oxidation and reduction processes, is rare-earth doped ceria. The prediction of the ionic conductivity of the electrolytes and a better understanding of the underlying atomistic mechanisms provide an important contribution to the future of sustainable and efficient energy conversion and storage. The central aim of this paper is the detailed investigation of the relationship between defect interactions at the microscopic level and the macroscopic oxygen ion conductivity in the bulk of doped ceria. By combining *ab initio* density functional theory (DFT) with Kinetic Monte Carlo (KMC) simulations, the oxygen ion conductivity is predicted as a function of the doping concentration. Migration barriers are analyzed for energy contributions, which are caused by the interactions of dopants and vacancies with the migrating oxygen vacancy. We clearly distinguish between energy contributions that are either uniform for forward and backward jumps or favor one migration direction over the reverse direction. If the presence of a dopant changes the migration energy identically for forward and backward jumps, the resulting energy contribution is referred to as *blocking*. If the change in migration energy due to doping is different for forward and backward jumps of a specific ionic configuration, the resulting energy contributions are referred to as *trapping*. The influence of both effects on the ionic conductivity is analyzed: blocking determines the dopant fraction where the ionic conductivity exhibits the maximum. Trapping limits the maximum ionic conductivity value. In this way, a deeper understanding of the underlying mechanisms determining the influence of dopants on the ionic conductivity is obtained and the ionic conductivity is predicted more accurately. The detailed results and insights obtained here for doped ceria can be generalized and applied to other ion conductors that are important for SOFCs and SOECs as well as solid state batteries.

Received 20th December 2017,
Accepted 2nd February 2018

DOI: 10.1039/c7cp08535d

rsc.li/pccp

1 Introduction

Increasing utilization of renewable energy sources like wind and solar power highlights the importance of energy conversion and storage. Solid oxide fuel cells (SOFC) have high energy conversion

efficiency and excellent fuel flexibility and are therefore a promising candidate for future energy applications. For good performance, an electrolyte with high oxygen ion conductivity is required.

Promising materials for solid electrolytes are rare-earth (RE) doped ceria $\text{Ce}_{1-x}\text{RE}_x\text{O}_{2-x/2}$,¹ which is investigated in this work, and other fluorite-type oxides like doped zirconia $(\text{ZrO}_2)_{1-x}(\text{RE}_2\text{O}_3)_x$ with dopants like RE = Sc, Yb, Er, Y, Dy, Gd, Eu and Nd or CaO,^{2,3} or doped hafnia $(\text{HfO}_2)_{1-x}(\text{RE}_2\text{O}_3)_x$ with dopants like Yb, Y and Sm.⁴ High oxygen ion conductivities were also reported for the perovskite-structured magnesium doped lanthanum or neodymium gallates $(\text{La}_{1-x}\text{Sr}_x\text{Ga}_{1-y}\text{Mg}_y\text{O}_{3-\delta})$ and $(\text{NdGa}_{1-y}\text{Mg}_y\text{O}_{3-\delta})$.⁵⁻⁷ Additional examples are the perovskite-structured rare-earth aluminates $\text{La}_{1-x}\text{Sr}_x\text{Al}_{1-y}\text{Mg}_y\text{O}_{3-\delta}$ for either Sr or Mg doping,⁸ the perovskite-structured calcium titanate $\text{CaTi}_{1-x}\text{Fe}_x\text{O}_{3-\delta}$ for Fe doping⁹ and the apatite-type $\text{La}_{10-x}\text{Ba}_x(\text{SiO}_4)_6\text{O}_{3-x/2}$.¹⁰

For all these systems, doping with lower valent oxides creates oxygen vacancies (*cf.* eqn (1)), which results for the vacancy jump mechanism in a significant increase in oxygen ion conductivity.

^a Institute of Physical Chemistry, RWTH Aachen University, Landoltweg 2, 52056 Aachen, Germany. E-mail: julius.koettgen@rwth-aachen.de, martin@rwth-aachen.de; Fax: +49 241 8092128; Tel: +49 241 8094712

^b Helmholtz-Institut Münster (IEK-12), Forschungszentrum Jülich GmbH, Corrensstr. 46, 48149 Münster, Germany

^c Frontier Research Institute for Materials Science (FRIMS), Nagoya Institute of Technology, Gokiso, Showa, Nagoya, Aichi 466-8555, Japan

^d Center for Materials Research by Information Integration (CMI²), Research and Services Division of Materials Data and Integrated System (MaDIS), National Institute for Materials Science (NIMS), 1-2-1 Sengen, Tsukuba, Ibaraki 305-0047, Japan

^e JARA-Energy, Forschungszentrum Jülich and RWTH Aachen University, Germany

^f JARA-HPC, Forschungszentrum Jülich and RWTH Aachen University, Germany

† Electronic supplementary information (ESI) available. See DOI: 10.1039/c7cp08535d

However, the ionic conductivity first increases and then decreases with increasing dopant fraction leading to an ionic conductivity maximum. The central aim of this paper is the detailed understanding of the underlying mechanism of the ionic conductivity maximum. In fact, an ionic conductivity maximum as a function of the doping fraction can also be found without the creation of oxygen vacancies for ionic conductors, *e.g.* for $(\text{Bi}_2\text{O}_3)_{1-x}(\text{Y}_2\text{O}_3)_x$,^{11–13} for mixed ionic–electronic conductors (MIEC), *e.g.* for Y-doped BSCF $(\text{Ba}_{0.5}\text{Sr}_{0.5}\text{Co}_{0.8}\text{Fe}_{0.2-x}\text{Y}_x\text{O}_{3-\delta})$,¹⁴ and for other types of ionic conductivity, *e.g.* for the proton conductivity in barium zirconate^{15–18} and Li-conducting NASICON materials.^{19–23} Due to an abundance of data, we have chosen rare-earth doped ceria as a model system in this work.

Pure cerium oxide itself is not a good ionic conductor.²⁴ However, doping for example with samarium oxide (Sm_2O_3) leads to high conductivities as revealed by impedance spectroscopy experiments. An ionic conductivity maximum as a function of

dopant fraction at $\text{Ce}_{0.8}\text{Sm}_{0.2}\text{O}_{1.9}$ was reported by Eguchi *et al.*²⁵ For different dopants ($\text{Ce}_{0.8}\text{RE}_{0.2}\text{O}_{1.9}$), a correlation between ionic conductivity and dopant radius²⁶ was found.^{25,27–29} Compared to nominally pure ceria, doping can also decrease the ionic conductivity *e.g.* by doping with Sc.³⁰

The influence of the type of dopant and the dopant fraction on conductivity has been a topic of research for half a century. Initially, analytical models were employed.^{31–34} For more than 30 years semi-empirical^{35–38} and since the turn of the 21st century *ab initio* calculations have been performed.^{39–43} Despite the development of various models, the detailed understanding of the underlying mechanism that determines the magnitude of the oxygen ion conductivity and the optimal dopant concentration is still missing.

In this work, this mechanism is closely investigated by presenting the relation between defect interactions and oxygen ion conductivity. Defect interactions are calculated using



Julius Koettgen

impedance spectroscopy measurements, density functional theory calculations and Kinetic Monte Carlo simulations.

Julius Koettgen studied Chemistry at the RWTH Aachen University, where he received his MSc degree with highest honours in 2012 and his PhD in 2017 under the supervision of Prof. Manfred Martin. He then continued at RWTH Aachen University as a post-doctoral researcher. His research interest focuses on the relation between defect interactions, local structure and oxygen ion conductivity using extended X-ray absorption fine structure and



Steffen Grieshammer

Steffen Grieshammer studied Chemistry at the universities in Oldenburg and Aachen and obtained his doctoral degree in chemistry at RWTH Aachen University in 2015 under the supervision of Prof. Manfred Martin. He then worked as a researcher at the Helmholtz-Institut Muenster and became young investigator group leader in 2016. His research focuses on computational investigation of solid state electrolytes using density functional theory and Monte Carlo methods.



Philipp Hein

non-stoichiometric oxide thin films and on the programming of Monte Carlo simulations for ion transport in solids.

Philipp Hein studied Chemistry at RWTH Aachen University in Germany, where he obtained his BSc in 2011 and his MSc degree with honours in 2013. Since then he is a PhD candidate in the group of Prof. Manfred Martin at the Institute of Physical Chemistry at RWTH Aachen University. Philipp's research interest is in the field of solid state chemistry and focuses both on experimental studies of novel resistive switching memories made from amorphous,



Masanobu Nakayama

research interests include experimental and computational studies on ion conducting materials for batteries and fuel cells. His other research interests include materials informatics to discover new compounds for batteries.

Masanobu Nakayama received his PhD from Tokyo Institute of Technology in 2004 under the supervision of Prof. M. Wakihara. He has been a Professor in the Department of Advanced Ceramics, Nagoya Institute of Technology, Japan since 2016. Also, he has been appointed as the group leader of Battery Materials Group, Materials research by Information Integration Initiative (M^2i), National Institute for Materials Science (NIMS), Japan. His

density functional theory (DFT) and oxygen ion conductivities are calculated using Kinetic Monte Carlo (KMC) simulations following our earlier publications.^{34,44–47} Only if both defect interactions and oxygen ion conductivities as well as their interdependency are known, the behavior in the bulk of doped ceria can be understood.

The paper is organized as follows: in Section 2, we review the investigated material doped ceria, its ionic conductivity according to the literature as well as the dopant fraction that leads to the highest conductivity. Subsequently, the corresponding activation enthalpies and interaction energies are discussed. Afterwards, we give a literature overview on interpretations of the conductivity data. In Section 3, we present our results for the defect interactions. Both the association energy between defects on regular lattice sites (trapping) and migration energies for the activation barriers of symmetric jump environments (blocking) are discussed. Afterwards, a model for the migration energy for all possible jump environments is presented. We classify migration energy models used in the literature and compare the quality of different models. In Section 4, we present our simulation results for the ionic conductivity including new experimental results with Sm doped ceria. By varying the amount of trapping or blocking for several dopants, the underlying mechanism that determines the magnitude of the oxygen ion conductivity and the optimal dopant concentration are investigated. Finally, we compare the calculations with experiments. In Section 5, we give a short conclusion. The theoretical, computational and experimental details are described in the appendix.

2 General background

2.1 Doped ceria

Doping of cerium oxide (CeO₂) with lower valent oxides, *e.g.* rare-earth oxides RE₂O₃, leads to the creation of oxygen vacancies¹ as shown in eqn (1) in the Kröger–Vink notation.



Manfred Martin

Manfred Martin studied Physics at the Technical University Hannover, where he received his Diploma (1978) and his PhD (1984). He continued as Lecturer in Hannover, obtained the Habilitation (1990) and was a Visiting Scholar at the University of Oxford before he received a full Professorship at Technical University Darmstadt in 1994. Since 2000, he has been Professor of Physical Chemistry at RWTH Aachen University. He

was a Visiting Professor at the University of California, Davis and is an Adjunct Professor at Seoul National University. His research focuses on defects and diffusion in solids using experimental and computational methods.

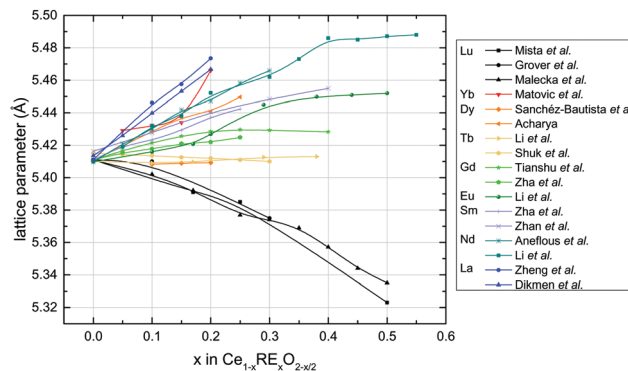


Fig. 1 Experimental lattice parameter of rare-earth doped ceria as a function of doping fraction. Measurements were performed in air at room temperature for Lu,^{63–65} Yb,⁶⁶ Dy,^{67,68} Tb,^{69,70} Gd,^{61,71} Eu,⁶⁹ Sm,^{71,72} Nd^{73,74} and La doped ceria.^{60,75} Lines are a guide to the eye only.

As dopant fractions in experiments are high (*cf.* Fig. 1), ceria is actually rather substituted than doped with rare-earth oxides.



As a result, rare-earth dopants (RE'_{Ce} or RE) and oxygen vacancies (V^{••}_O or V) are the majority defects with a concentration controlled by the dopant fraction according to $[\text{RE}'_{\text{Ce}}] = 2[\text{V}^{\bullet\bullet}_{\text{O}}]$ for Ce_{1-x}RE_xO_{2-x/2}. Other defects can be neglected and the concentration of oxygen vacancies is independent of temperature. In this work, dopant fractions are given as RE₁O_{1.5} mol%, though in the literature RE₂O₃ mol% is also used.

It is known that under oxygen poor conditions ceria can be reduced leading to the formation of polarons,^{48,49} and a number of theoretical studies have been dedicated to this subject.^{50–56} However, we restrict our simulations to conditions where the electronic conductivity is significantly smaller than the ionic conductivity and thus can be neglected.

Doping is limited by solubility. While for some dopants solubility above $x = 0.4$ has been reported,¹ contradicting information about the solubility limits is found in the literature as described in the following. Often X-ray diffraction analysis cannot identify the development of secondary phases, as they are very similar to the fluorite structure of ceria. For the dopants investigated in this work, most studies report solubility up to about $0.2 < x < 0.6$ (*cf.* Fig. 1),^{57,58} *e.g.* Balazs and Glass found for $x = 0.2$ minor impurity phases for small (Lu, Yb, Tm) and large dopants (Nd, La) compared to Ce⁴⁺.⁵⁹ For the even smaller dopant Sc, the solubility limit is already reached at 3–5%.^{1,30} For the large dopant La, the solid solution Ce_{0.8}La_{0.2}O_{1.9} appears to be only metastable as decomposition is observed after sintering for seven days at high temperature.^{60,61} For Y, Gd and Sm doped ceria, solubility of at least $x = 0.3$ up to complete miscibility is reported.^{57,62}

The lattice parameter of doped ceria depends on the ionic radius of the dopant. For Ce_{0.8}RE_{0.2}O_{1.9}, the lattice parameter changes linearly with the dopant radius obeying Vegard's law.^{25,27,59,76} Fig. 1 shows that the lattice parameter decreases (for small dopants) or increases (for large dopants) with increasing

dopant fraction until a constant value is reached, which indicates the solubility limit.^{60,74} For Yb, Dy and Eu doped ceria, a few deviations from this rule can be found. Earlier measurements for several dopants from Brauer and Gradinger indicated lower lattice parameters than those shown in Fig. 1.⁷⁷ Some studies even assume a relationship between the association of oxygen vacancies with dopants and the deviation of Vegard's law of the linear relationship between the lattice parameter and the dopant fraction.^{58,61,69,78}

2.2 Ionic conductivity

In this work, the migration of oxygen vacancies in fluorite-structured ceria is considered between adjacent tetrahedral oxygen sites in the (100) direction, as other migration paths possess a significantly higher jump barrier,⁴⁴ with a jump distance given by half of the unit cell length.¹ Along this pathway two cations form a 'migration edge' through which the migrating oxygen has to pass. In pure CeO₂, only cerium ions are at the migration edge, while doping with rare-earth (RE) oxide leads to configurations with one or two RE ions at the migration edge (see Fig. 2). An undoped migration edge is called Ce–Ce edge. If rare-earth dopants (RE) are present, the labels Ce–RE edge or RE–RE edge are used.

In this subsection, ionic conductivities for oxygen ion migration in doped ceria according to experiments are reviewed. For polycrystalline samples, the total conductivity is influenced by the bulk and grain boundary domains. In the bulk domain, oxygen ions jump through the regular lattice. In the grain boundary domain, jumps take place along or across dislocations and in space charge zones and are hindered due to the depletion of oxygen vacancies.⁷⁹ The separation of both domains is possible using *e.g.* impedance spectroscopy measurements where two semi-circles are observed in the Nyquist plot. For the conductivity measurements reported in this work, the electronic contribution to conductivity is negligible.^{1,80} As shown exemplarily by Steele,⁸⁰ the total conductivity is determined by the bulk and grain boundary conductivities, which have conductivity maxima at different dopant fractions. For small dopant fractions, the total conductivity is limited by the low grain boundary conductivity. For large dopant fractions, the conductivity is limited by the low bulk conductivity. Compared to the total domain, the dopant fraction leading to the maximum in conductivity x_{\max} is small for the bulk conductivity.⁸⁰ The bulk domain is of particular interest as it represents the inherent property of the doped material largely without the influence of the microstructure of the sample.⁸¹ Therefore, we focus only on the ionic conductivity of the bulk in this work.

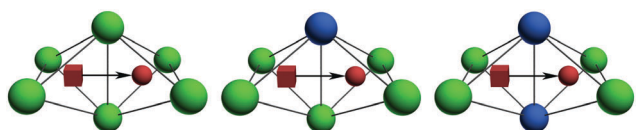


Fig. 2 Possible migration edge configurations for the migration of oxygen in rare-earth (RE) doped ceria. Ce–Ce edge (left), Ce–RE edge (middle) and RE–RE edge (right). Cerium ions (green), rare-earth ions (blue), oxygen ions (red spheres) and oxygen vacancies (red boxes).

The bulk conductivity depends significantly on the type of dopant and the investigated temperature. Faber *et al.* measured the bulk ionic conductivity of Yb, Y, Gd, Nd and La doped ceria between 30 °C and 330 °C.⁸⁶ For small dopant fractions, Nd doped ceria possesses the highest bulk conductivities, where a maximum appears at $x_{\max} = 0.03$ (Table 1). For large dopant fractions, Gd doped ceria possesses the highest bulk conductivities, where a maximum appears at $x_{\max} = 0.06$ –0.18. Nowick *et al.*¹⁰² reported for Y doped ceria at 181 °C similar conductivities as those reported by Faber *et al.* The dopant fraction leading to the maximum in conductivity x_{\max} decreases with increasing dopant radius at low temperature. Here, often the ionic radii according to Shannon are given.²⁶ The relation between the conductivities of different dopants is similar for all measured temperatures.

For 500 °C, a summary of several experiments is shown in Fig. 3. A strong scattering between the experiments of different research groups is found. The dopant fractions leading to the maximum in conductivity differ significantly (Table 1).

For all temperatures, the dopant fraction leading to the maximum in conductivity is found between $x_{\max} = 0.02$ and 0.38 (Table 1 and Fig. S1, ESI†). For all dopants, at least one reference is found with a dopant fraction leading to the maximum in conductivity of about $x_{\max} = 0.1$. The distribution of x_{\max} is broad especially for medium ionic radii, which lead to the highest conductivities. The measured temperature range and x_{\max} correlate. Measurements at low temperature rather lead to low x_{\max} , while measurements at high temperature rather lead to high x_{\max} (*cf.* Fig. S1, ESI†). Additionally, the conductivity for a single dopant fraction can be investigated. For all dopant fractions, a general initial increase and a subsequent

Table 1 Dopant fractions that lead to the highest bulk ionic conductivity for Ce_{1-x}RE_xO_{2-x/2} samples in the measured temperature range

Dopant	x_{\max}	Temperature (°C)	Ref.
Yb	0.08	30–330	Faber <i>et al.</i> ⁸⁶
Y	0.08	181	Nowick <i>et al.</i> ¹⁰²
	0.08	80–200	Wang <i>et al.</i> ⁸⁴
	0.08	80–330	Faber <i>et al.</i> ⁸⁶
	0.08	500–700	Tian and Chan ^{103,104}
Gd	0.06	30	Faber <i>et al.</i> ⁸⁶
	0.10	80	
	0.18	130–330	
	0.10	500	Steele ⁸⁰
	0.10	350–450	Tianshu <i>et al.</i> ⁶¹
	0.20	450–500	
Eu	0.38	400–600	Li <i>et al.</i> ⁶⁹
Sm	0.1	250–550	Zhan <i>et al.</i> ⁷²
	0.15	500–700	Sanghavi <i>et al.</i> ⁹⁷
Nd	0.10	300–500	Zhu <i>et al.</i> ¹⁰¹
	0.20	500–800	
	0.03	30–280	Faber <i>et al.</i> ⁸⁶
	0.10	330	
La	0.02	30–170	Faber <i>et al.</i> ⁸⁶
	0.10	170–330	

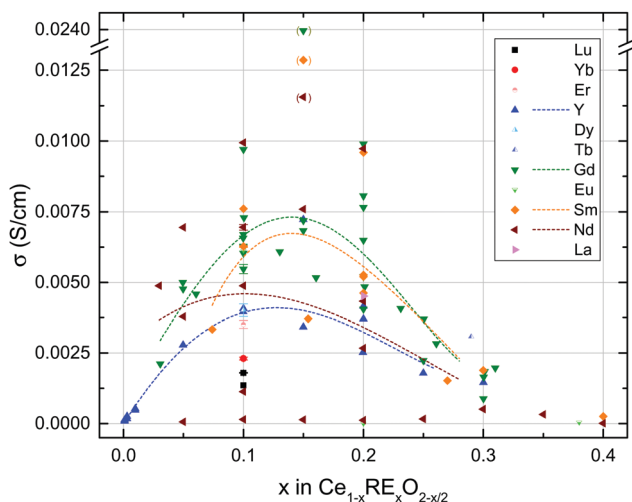
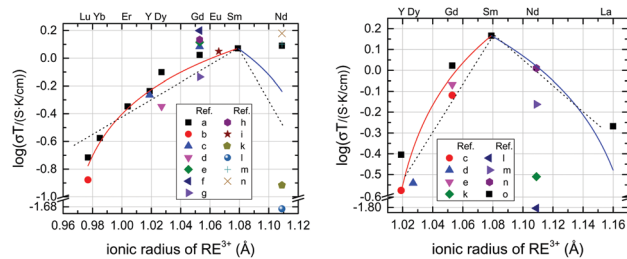


Fig. 3 Bulk ionic conductivity of rare-earth doped ceria as a function of doping fraction. Measurements were performed in air at 500 °C for Lu,^{82,83} Yb,⁸³ Er,⁸³ Y,^{83–90} Dy,⁸³ Tb,⁶⁹ Gd,^{61,80,83,87–95} Eu,^{69,96} Sm,^{72,83,87–90,97–99} Nd^{73,74,83,88,100,101} and La doped ceria.⁸⁷ Fourth order polynomials are fitted to the data as a guide to the eye only (dashed lines) with the exception of the data of Zajac and Molenda (in parentheses), which were disregarded due to the strong deviation compared to other literature data.

decrease in conductivity with increasing dopant radius is found with a maximum around Gd and Sm doped ceria. For example, Mogensen *et al.*¹⁰⁵ found for $x = 0.1$ in $\text{Ce}_{1-x}\text{RE}_x\text{O}_{2-x/2}$ at 1000 °C the highest conductivity for the dopant RE = Gd and lower conductivities for the smaller dopants Sc and Y as well as for the larger dopant La. Omar *et al.*⁸³ investigated Lu, Yb, Er, Y, Dy, Gd, Sm, and Nd doped ceria ($x = 0.1$) and found for 400–600 °C an increasing conductivity with increasing dopant radius, which is in disagreement with the other studies. Zajac⁸⁸ studied Y, Gd, Sm and Nd doped ceria ($x = 0.15$) at 700 °C where Gd doped ceria has the highest conductivity. Pérez-Coll *et al.*⁸⁷ investigated Y, Gd, Sm and La doped ceria ($x = 0.2$) and found for 200–700 °C the highest conductivity for Sm doped ceria.

In Fig. 4, the bulk conductivity at 400 °C for $x = 0.1$ and 0.2 is extracted. For $x = 0.2$, doping with Sm leads to the highest bulk ionic conductivity. For $x = 0.1$ the conductivity of Gd, Eu, Sm and Nd doped ceria is similar. As often presented in the literature, the dashed lines show a linear relationship in sections (volcano-type) between the ionic radius and the logarithm of the bulk conductivity. Additionally, in this work, we show a linear relationship between the ionic radius and the bulk conductivity with solid lines. Both relationships cannot be clearly verified due to strong scattering, especially for Nd doped ceria. A fit is shown with the red line, while the blue line and the dashed lines are a guide to the eye only.

Finally, it is surprising, as shown in Fig. 3, that only a few dopant fractions of Sm doped ceria were examined despite its high conductivity. Polycrystalline samples were analyzed for $x = 0.1, 0.2$ and 0.3 ,^{72,83,87,89,90,98,99} or 0.15 ,⁸⁸ while Sanghavi *et al.*⁹⁷ investigated single crystal thin films for a few dopant fractions. For a complete picture, a detailed concentration series of Sm doped ceria was investigated in this work and the results will be presented in Section 4.



(a) Experiments for $x = 0.1$

(b) Experiments for $x = 0.2$

Fig. 4 Bulk ionic conductivity of rare-earth doped ceria as a function of dopant radius. Measurements were performed in air at 400 °C for $\text{Ce}_{1-x}\text{RE}_x\text{O}_{2-x/2}$ with $x = 0.1$ and 0.2 according to references a,⁸³ b,⁸² c,⁸⁵ d,⁶⁷ e,⁶¹ f,¹⁰⁶ g,⁹² h,⁹⁵ i,⁹⁶ k,⁷⁴ l,⁷³ m,¹⁰⁰ n,¹⁰¹ and o.⁸⁷ The lines show a linear relationship between the ionic radius and the conductivity (solid lines) or the logarithm of the conductivity (dashed lines).

2.3 Activation enthalpy

The temperature dependent behavior of the bulk conductivity in doped ceria can be shown in an Arrhenius plot according to

$$\sigma = \frac{A}{T} e^{-\frac{\Delta H_a}{k_B T}} \quad (\text{see Appendix: theoretical details}).$$

Most literature sources derive an (apparent) activation enthalpy ΔH_a from a linear relationship between $\ln(\sigma T)$ and $1/T$: the activation enthalpy for rare-earth doped ceria was extracted by Faber *et al.*⁸⁶ from measurements between room temperature and 330 °C for several dopants and by many other research groups from measurements up to 1000 °C for Lu,^{82,83} Yb,⁸³ Er,⁸³ Y,^{83–85,87,88,98} Dy,^{67,83} Gd,^{61,83,85,87,88,91,92,94} Eu,⁹⁶ Sm,^{72,83,88,98,107} Nd^{74,83,88,100,101} and La doped ceria,⁸⁷ which will be compared to simulations in Fig. 25. It should be noted that in experiments generally the activation enthalpy is extracted while static calculations only give the electronic energy.⁴⁷ Both can be compared as described in our earlier publication.¹⁰⁸

Activation enthalpies scatter significantly, *e.g.* between 0.63 eV and 0.82 eV for $\text{Ce}_{0.9}\text{Gd}_{0.1}\text{O}_{1.95}$ and between 0.80 eV and 0.94 eV for $\text{Ce}_{0.8}\text{Gd}_{0.2}\text{O}_{1.9}$. For Sm and Nd doped ceria, activation enthalpies scatter between 0.46 eV and 0.72 eV for $\text{Ce}_{0.9}\text{Sm}_{0.1}\text{O}_{1.95}$ and between 0.65 eV and 0.82 eV for $\text{Ce}_{0.9}\text{Nd}_{0.1}\text{O}_{1.95}$.

In the experimental literature, activation enthalpies first decrease and then increase as a function of dopant fraction, similar to other fluorite-structured oxides.³³ For example, a decrease between $x = 0.001$ and 0.02 was found for Y or Nd doped ceria.^{84,100} An increase between $x = 0.03$ and 0.4 was found for Sm, Y, Gd or Nd doped ceria.^{72,85,100} Faber *et al.*⁸⁶ found minima in the activation enthalpy at $x = 0.02$ –0.04 (for Nd), 0.08 (Yb), 0.04 (Y), 0.06 (Gd) and 0.02 (La).

For a single dopant fraction, the activation enthalpy decreases for an increasing dopant radius up to the dopants Gd, Eu, Sm and Nd and increases afterwards. For example, Faber *et al.*⁸⁶ investigated Yb, Y, Gd, Nd and La doped ceria where Nd doped ceria has the lowest activation enthalpy. Omar *et al.*⁸³ investigated Lu, Yb, Er, Y, Dy, Gd, Sm, and Nd doped ceria ($x = 0.1$) and found for Sm doped ceria the lowest ΔH_a , similar to Zajac,⁸⁸ who investigated Y, Gd, Sm and Nd doped ceria ($x = 0.15$). Pérez-Coll *et al.*⁸⁷ investigated Y, Gd, Sm and

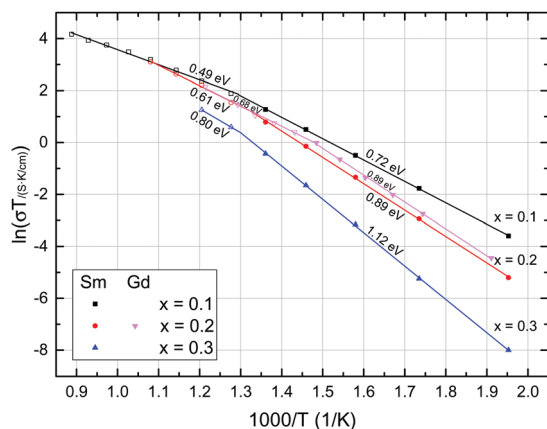


Fig. 5 Bulk ionic conductivity of $\text{Ce}_{1-x}\text{RE}_x\text{O}_{2-x/2}$ as a function of temperature. Measurements were performed for Sm and Gd doped ceria by Zhan *et al.*⁷² and Zhang *et al.*⁸⁵ A low and a high temperature region can be found with different activation enthalpies.

La doped ceria ($x = 0.2$) and also found the lowest ΔH_a for Sm doped ceria.

Furthermore, several groups find different activation enthalpies for low and high temperatures (see Fig. 5). Here, the resulting ΔH_a is high for the low temperature region and low for the high temperature region. This leads to a kink in the Arrhenius plot around 350–600 °C.^{72,83,85,87,92,99,100,107} The difference in activation enthalpy between low and high temperature regions is often interpreted as ‘apparent association enthalpy’ or ‘apparent association energy’ between an oxygen ion and rare-earth dopant or an $(\text{RE}'_{\text{Ce}}\text{V}_{\text{O}}^{\bullet\bullet})^{\bullet}$ associate. In the following, we will use the more commonly used term association energy, even though experiments actually give the association enthalpy. We will show that the assumption of a single RE–V association energy neglects other interactions which appear during the oxygen migration. Furthermore comparison of literature results shows that the apparent association energies for a single dopant vary. While Omar *et al.* find apparent association energies between only 0.02 and 0.05 eV for different dopants⁸³ and other groups find no kink in the Arrhenius plot, Gerhardt-Anderson and Nowick determine the apparent association energy for Sc doped ceria to be 0.67 eV.³⁰ It should be noted that Wang *et al.* as well as Gerhardt-Anderson and Nowick determine the apparent association energy by assuming a value for the activation enthalpy at high temperature (0.61 eV), which is estimated using an experimental investigation of nominal pure ceria and the expected Ca impurity concentration of the material. Zhang *et al.* use the same method with an activation enthalpy at high temperature of 0.63 eV.⁸⁵ Stephens and Kilner use the lowest migration energy of different dopant fractions as a reference to calculate the apparent association energy.¹⁰⁰ The apparent association energies are shown in Fig. S2 (ESI[†]). From $x = 0.001$ to 0.02 a decrease in apparent association energy for Y doped ceria was found.⁸⁴ The same is true for Nd doped ceria from $x = 0.01$ to 0.03.¹⁰⁰ From $x = 0.03$ to 0.4 an increase in apparent association energy for Y, Gd, Sm

and Nd doped ceria was found.^{72,84,85,100} Therefore, a minimum for the apparent association energy as a function of the dopant fraction was reported.

2.4 Proposed origins of the conductivity maximum

The oxygen ion conductivity increases steeply with increasing dopant fraction of the trivalent rare-earth dopant to a maximum at mostly $x_{\text{max}} = 0.08\text{--}0.2$ and then decreases gently. In the following, interpretations according to the literature are summarized.

The initial rise in oxygen ion conductivity with increasing dopant fraction is caused by the creation of oxygen vacancies according to eqn (1).³¹ If no further interactions existed, the ionic conductivity would increase to a maximum until half of the oxygen sublattice is unoccupied according to $\sigma \propto x(1-x)$.¹⁰⁹ In experiments, the maximum in conductivity appears at significantly lower dopant fractions. According to the literature, the position of the maximum clearly depends on the number of oxygen vacancies,[‡] which are created per dopant, as in Ca^{2+} or Sr^{2+} doped ceria the maximum appears at lower dopant fractions.^{1,110–113} The reasons given for the decrease in conductivity are the association between oxygen vacancies and dopants, the ordering of oxygen vacancies or a modified jump probability of the oxygen vacancies.

In most of the literature, it is commonly assumed that the maximum in oxygen ion conductivity is only caused by the association between oxygen vacancies and dopants. The association originates from the Coulomb interaction of the defects and local relaxation of the crystal lattice. In this work, electronic migration energies are used to describe the microscopic jump process according to an earlier work¹⁰⁸ rather than activation enthalpies. The migration energies for vacancy jumps away from the associating dopant (dissociative jumps) are higher than in pure ceria, while jumps to the dopant are favored (associative jumps). These jump configurations are shown in Fig. 6. In simple terms it is often described that the oxygen vacancies are trapped or immobilized by the almost immobile dopants and thereby the concentration of the free vacancies is reduced.§ Several experiments and calculations support this picture.

In experimental measurements of the ionic conductivity or the diffusion coefficient, it is assumed that the high-temperature and low-temperature regimes differ in activation enthalpy by the apparent association energy between the migrating oxygen vacancy and the dopant as described above. While at low temperature vacancies are trapped, at high temperature sufficient energy is available to free the vacancies, which leads to a decrease in apparent activation enthalpy.^{30,72,84} However, activation enthalpies at high temperature still depend on the dopant fraction^{72,100} and type of dopant.⁸³ This indicates that the assumption is restricted and might only be correct in dilute solutions as discussed in the literature.^{84,114} In general, semi-empirical^{36,37} and *ab initio*^{41,42}

‡ However, for Ca^{2+} doped ceria for example, the association energy and the jump barriers around Ca^{2+} differ significantly compared to most rare-earth dopants, which is rarely discussed in the literature.

§ This picture is an oversimplification as vacancies are not trapped for an infinitely long duration.

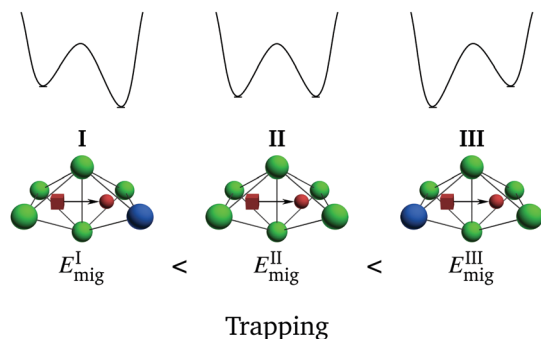


Fig. 6 Migration configurations in rare-earth doped ceria. The upper diagram shows the energy of the system as a function of the reaction coordinate for the configuration change that is shown below. For colours, see Fig. 2. The migration energy increases if the oxygen ion jump weakens the association between the oxygen vacancies and the dopants.

calculations can be used to support the picture of the apparent association energies found in conductivity measurements. Schmalzried used electrostatic interactions, which lead to different probabilities for forward and backward jumps, to describe a relationship between increasing activation energies and increasing dopant fraction.³²

The formation of associates is also found in other experiments: neutron diffraction experiments of yttria-stabilized zirconia (YSZ) show not only sharp Bragg reflections but also a background that is modulated with the scattering vector. This diffuse scattering indicates the presence of not completely ordered atoms such as oxygen ions, which are moved towards the vacancies, or possibly associates of dopants and vacancies.¹¹⁵ Electron spin resonance spectroscopy suggests that charged defect complexes of dopants and an oxygen vacancy $(\text{RE}'_{\text{Ce}}\text{V}_{\text{O}}^{\bullet})^{\bullet}$ exist at low dopant fractions.¹¹⁶ Extended X-Ray Absorption Fine Structure (EXAFS) measurements of the coordination numbers of cations and anions confirm the formation of associates.^{117–120} Finally, Nuclear Magnetic Resonance (NMR) measurements support the formation of associates for ⁴⁵Sc doped ceria,¹²¹ ⁸⁹Y doped ceria,^{121–123} and ¹³⁹La doped ceria.¹²⁴

While the formation of associates is commonly accepted, the dopant fraction at which associates emerge and influence the conductivity is a topic of discussion. Early approaches assumed that discrete localized clusters separated from the ideal cerium lattice are present and that their concentration can be described using equilibrium thermodynamics.³⁰ However, this model failed at larger dopant fractions because no further interactions are considered.⁸⁴ Besides association, research groups presume the formation of *defect clusters*^{28,92} or *nanoscale domains*: especially at high dopant fractions, Tien and Subbarao,¹²⁵ Nakamura,^{126,127} Ou *et al.*^{128,129} and Hooper *et al.*¹³⁰ reported an ordering of the oxygen vacancies leading to reduction of the oxygen ion conductivity.

While the association and ordering of defects can be investigated experimentally, the influence of both phenomena on the oxygen ion migration can only be speculated on. Thus, many investigations show that attractive and repulsive interactions

are not sufficient to describe the experimental results without considering *modified jump probabilities* or migration energies.

Murray and Murch determined the oxygen ion conductivity using Kinetic Monte Carlo (KMC) simulations and explained the maximum in conductivity as a function of the dopant fraction.³⁸ For this purpose, they used migration energies for oxygen ion jumps depending on the local environment, which were calculated using empirical potentials. Here, jump environments with the same distance between a dopant and the migrating oxygen vacancy before and after a jump possess different migration energies than jumps in pure ceria. Murray and Murch found for high dopant fractions that oxygen vacancies jump mostly in the vicinity of dopants. Therefore, they do not contribute to the oxygen ion transport through the crystal and the ionic conductivity decreases.

Shimojo *et al.* deduced from molecular dynamics simulations of yttria-stabilized zirconia (YSZ) using empirical potentials that the ionic conductivity is less influenced by the $\text{Y} - \text{V}_{\text{O}}^{\bullet}$ associates, but rather by lower jump probabilities of oxygen ions around Y dopants.¹³¹ Indeed, it is rarely discussed that doping leads to migration configurations, where oxygen vacancies and dopants have the same distance before and after a jump. These configurations possess a symmetric jump profile: initial and final states are energetically equivalent. Forward and backward jumps have the same migration energies. For large dopants, the migration is typically hindered, *i.e.* the oxygen ion is blocked. Migration energies increase for an increasing number of large dopants at the migration edge as illustrated in Fig. 7. Meyer and Nicoloso showed using KMC simulations that the interactions between nearest neighbors of oxygen vacancies and dopants on regular lattice sites are not sufficient to calculate the oxygen ion conductivity, but rather that a migration energy model is required.¹³² In 2006, we showed using an analytical model that the combination of nearest neighbor interaction and reduced jump probabilities could explain qualitatively the experimental findings.³⁴

The question remains whether immobilized vacancy–dopant associates, an ordering of the vacancies and modified jump

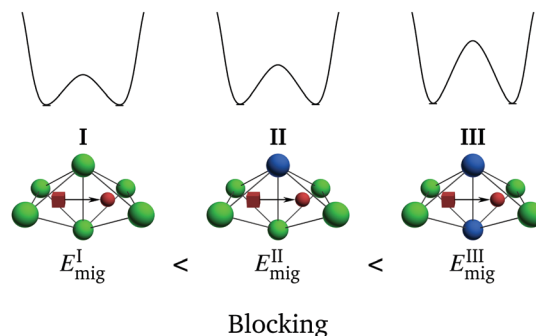


Fig. 7 Migration configurations in rare-earth doped ceria according to Fig. 2. The upper diagram shows the energy of the system as a function of the reaction coordinate for the configuration change that is shown below. The migration energy increases for an increasing number of large dopants at the migration edge.

probabilities influence the ionic conductivity separately, simultaneously or are mutually dependent.

2.5 Proposed origins of the change in conductivity for different dopants

The oxygen ion mobility depends not only on the dopant fraction but also on the type of dopant. First theories postulated that the highest oxygen ion conductivity occurs for dopants with the least distortion of the crystal lattice.³¹ In 1981, Wang *et al.*⁸⁴ and Gerhardt-Anderson and Nowick³⁰ suggested that the optimal dopant has the ionic radius of the Ce⁴⁺-cation. However, in the next 15 years, different dopant radii leading to the least distortion of the crystal lattice were proposed.^{1,28,133–136}

Alternatively, the influence of different dopants on the ionic conductivity is attributed to the formation of *associates*. In experiments, EXAFS measurements show the formation of oxygen vacancy–dopant associates based on the coordination numbers or the distances between anions and cations. Here, dopants, which lead to high oxygen ion conductivities like Sm and Gd, involved less formation of associates than other dopants like Y or La.^{119,120,137} However, some EXAFS measurements deviate from this rule.¹¹⁸ NMR measurements confirm a stronger association between Sc dopants and oxygen vacancies compared to Y dopants and oxygen vacancies.¹²¹ Association energies derived from early impedance experiments and calculations using potentials of the Born–Mayer form show that dopants, which lead to high oxygen ion conductivities, possess lower association energies (Fig. S2, ESI[†]).^{30,36,37} Here, oxygen vacancies are less trapped by dopants and have higher mobility. According to previous reports, the strong association for small dopants (*e.g.* Sc) is based on Coulomb interactions, while large dopants (*e.g.* La) form associates due to minimal stress in the crystal lattice.¹ These opposed effects should lead to the minimal association energy for Gd doped ceria.

However, subsequent experiments demonstrated that apparent association energies scatter or activation enthalpies are even temperature independent and the ionic conductivity exhibits no kink in the Arrhenius plot (see Section 2.3). Apparent association energies depend on the dopant fraction with a minimum around $x = 0.03$. For Sm doped ceria, large apparent association energies are reported despite its high ionic conductivity (Fig. S2, ESI[†]). Later, empirical¹³⁸ and *ab initio* calculations^{41,44,46} showed that the association energy decreases with increasing ionic radius up to La. These and further calculations also show that, for large dopants, oxygen vacancies no longer reside in closest possible proximity to the dopants (nearest neighborhood, 1_{NN}), but in the next-adjacent location (next nearest neighborhood, 2_{NN}).^{139,140} The latter is in contrast to calorimetric measurements of La doped ceria where vacancies were found to remain predominantly in the nearest neighborhood to the trivalent dopant.¹⁴¹ Clearly, the microscopic association between dopants and oxygen vacancies and the macroscopic apparent association energy *e.g.* derived from impedance experiments are connected. However, microscopic and macroscopic processes are not equivalent. The macroscopic conductivity is a thermodynamic average of all jumps occurring in the solid. In this work, Kinetic Monte Carlo (KMC) simulations are used to link both processes.

Furthermore, theoretical studies show that, besides association, other *modified jump probabilities* for different dopants exist. For example, we calculated migration energies for variously doped ceria using density functional theory (DFT) in 2009.⁴⁴ However, for similar migration configurations, the variation of the type of dopant leads to different trends in the literature.^{41,142–145} The origins of these discrepancies are investigated in this work.

If the dopant fraction or the type of dopant is varied, experiments suggest a relationship between conductivity and apparent activation enthalpy. It has been suggested that the maximum in conductivity correlates with a minimum in activation enthalpy as a function of dopant fraction and dopant type. Wang *et al.*^{84,102} showed for Y doped ceria that the maximum of the conductivity at 182 °C for different dopant fractions occurs at similar compositions as the minimum in activation enthalpy. The same applies to the data of Faber *et al.*⁸⁶ with the best dopants Gd and Nd and to the data of Pérez-Coll *et al.*⁸⁷ with the best dopant Sm. Mori *et al.* reported as well that the activation enthalpy mirrors the maximum in the conductivity for several dopant fractions in Gd doped ceria.¹⁴⁶ Deviations from this trend are shown by Omar *et al.*⁸³ and Zajac.⁸⁸ Similar to the association energy, microscopic migration energies and macroscopic activation enthalpies are connected. In this work, again KMC simulations are used to link both processes.

3 Trapping and blocking

In this section, we describe the defect interactions and their influence on the migration energy. In doped ceria, rare-earth dopants (RE) and oxygen vacancies (V) are introduced as point defects and a vast amount of possible ionic configurations around any oxygen ion jump exists. Especially the interactions between dopants and vacancies (RE–V association) as well as the interactions between vacancies (V–V repulsion) influence the migration energy. In this work, a model is developed to predict migration energies for all possible jump configurations in doped ceria. For this purpose, migration barriers are investigated for energy contributions that are energetically symmetric for both migration directions, *i.e.* the energy contribution is identical for forward and backward jumps, as well as energetically asymmetric for forward and backward jumps. Both cases were already discussed in Section 2.4. Positive symmetric contributions, relative to pure ceria, increase the migration energy for both forward and backward jumps similarly. While the equilibrium defect distribution is independent of these symmetric contributions, oxygen vacancies are kinetically hindered and therefore blocked (*blocking*). Positive asymmetric contributions lead to a larger migration barrier for the forward jump away from a dopant but a smaller migration barrier for the backward jump. The defect distribution is significantly influenced. Vacancies reside more often in the neighborhood to the dopant (*trapping*).

As a first example, only the six nearest cation sites around an oxygen vacancy jump are considered, the ‘6-cation environment’ (see Fig. 2). The two cation sites forming the migration edge have the same nearest neighborhood distance to the oxygen

vacancy before and after the jump ($1_{\text{NN}} \leftrightarrow 1_{\text{NN}} \text{ RE-V}$, see Fig. 7) and are nearest to the migrating oxygen ion in the transition state. We define this type of dopant position as geometrically symmetric. The other two cation site pairs are near to either the initial or final position of the migrating oxygen vacancy. These sites are referred to as $1_{\text{NN}} \rightarrow 2_{\text{NN}} \text{ RE-V}$, *i.e.* the oxygen vacancy is in 1_{NN} position to the dopant in the initial and 2_{NN} in the final position of the jump, or $2_{\text{NN}} \rightarrow 1_{\text{NN}} \text{ RE-V}$, accordingly. We define this type of dopant position as geometrically asymmetric.

It seems likely that geometrically symmetric jump configurations lead to symmetric energy contributions to the migration barrier and also that geometrically asymmetric jump configurations lead especially to asymmetric energy contributions to the migration barrier. Therefore, we investigated the migration energy of symmetric jump configurations for a blocking effect and the energy difference between the final and the initial state, which is referred to as interaction energy, of geometrically asymmetric jump configurations for a trapping effect.

Initially, we assume that the influence of the cation and anion sublattice on the migrating oxygen ion can be separated. This means that RE-V and V-V interactions have the same influence on the migration energy whether they occur either individually or simultaneously. Additionally, as few defects as possible are used to calculate parameters for the migration energy model since long-range Coulomb interactions lead to the repulsion of the defects and their copies due to the periodic boundary conditions, which are applied in density functional theory (DFT) calculations. In this work, energies are extrapolated to an infinitely large supercell to minimize interactions and dependencies on the supercell size. Subsequently, the model is tested *versus* defect-rich cells with experimental defect concentrations.

3.1 Trapping: interaction energy

3.1.1 RE-V association energy. In this work, the attractive 1_{NN} and 2_{NN} RE-V association energies, which cause the trapping of vacancies near dopants, were calculated in $2 \times 2 \times 2$ and $3 \times 3 \times 3$ supercells containing 95 and 323 atoms, respectively. RE-V association energies in Fig. 8 are given relative to the 3_{NN} RE-V association energy, according to $\Delta E_{\text{RE-V}}^1 = E(1_{\text{NN}}) - E(3_{\text{NN}})$ and $\Delta E_{\text{RE-V}}^2 = E(2_{\text{NN}}) - E(3_{\text{NN}})$, where $E(x_{\text{NN}})$ is the energy of the supercell with a x_{NN} RE-V distance. Further energy differences are small, *e.g.* $\Delta E_{\text{Sm-V}}^4 = E(4_{\text{NN}}) - E(3_{\text{NN}}) < 0.02 \text{ eV}$ in a $3 \times 3 \times 3$ supercell, and is set to zero in this work. Therefore, the RE-V association energy is 'terminated' at 3_{NN} . Using the finite size correction according to Makov and Payne (see Appendix: computational details), energies for an infinitely large supercell are obtained ('inf'). For comparison, the Coulomb energy was calculated

$$E_{\text{Coulomb}} = \frac{q_1 \cdot q_2}{4\pi\epsilon_0\epsilon_r r} \quad (2)$$

with the charges q_1 and q_2 of the defects compared to an ideal lattice according to eqn (1), the dielectric constant for vacuum ϵ_0 , the relative dielectric constant for pure ceria ϵ_r of about 25, which was calculated using DFT, and the defect distance r . Similar to the DFT calculations, the Coulomb energy is given relative to the Coulomb energy at 3_{NN} . The relative Coulomb

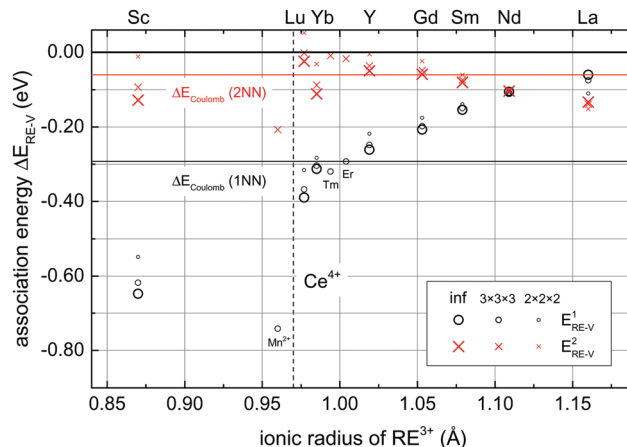


Fig. 8 RE-V interaction energy as a function of the ionic radius of RE^{3+} . Different supercell sizes are calculated under the assumption of $\Delta E_{\text{RE-V}}^3 = 0$ (see text). The horizontal lines indicate the classical Coulomb energies for the nearest neighbor and next nearest neighbor distances, which are calculated for an ideal lattice geometry.

energy possesses a value that is in the range of the calculated association energies. The reasons for the broad distribution of the calculated association energies are local lattice relaxations and different electron densities. These effects lead to large differences between the association energies of different dopants as already reported in the literature.^{41,44,142–145}

Fig. 8 shows a monotonous decrease of the absolute value of the 1_{NN} RE-V association energy with increasing dopant size. For the absolute value of the 2_{NN} association energy, a minimum is found for the Lu-V association. An energetically preferred 1_{NN} association is found for small dopants (*e.g.* Sc), while for the large dopant La the 2_{NN} association is preferred, in agreement with the literature.^{41,44,46,145} Mn^{2+} and Yb^{3+} show deviation from this behavior. However, Mn is not a rare-earth element and has a different charge state and was only chosen as it has a similar ionic radius as Ce^{4+} . In addition, the applied PAW-GGA-PBE potential (see Appendix: computational details) for ytterbium is optimized for Yb^{2+} .

In Fig. 8, the results for the $2 \times 2 \times 2$, the $3 \times 3 \times 3$ and the extrapolated supercell are shown. For dopants smaller than Nd, the absolute value of the association energy increases with increasing cubic supercell sizes. Lu dopants and oxygen vacancies even repel each other on the next nearest neighbor position (2_{NN}) in a $2 \times 2 \times 2$ supercell. The Nd-V association energy is independent of the supercell size. For Nd, the 1_{NN} and 2_{NN} RE-V association energies are also identical. The absolute value of the La-V interaction energy increases for smaller cubic supercell sizes. All these supercell-size-dependent effects emphasize the need for extrapolation of the association energy to an infinitely large supercell to mitigate finite size effects.

Lu^{3+} and Mn^{2+} have a similar ionic radius as Ce^{4+} . Therefore, it could be assumed that their strong association with oxygen vacancies is not caused by elastic contributions, *i.e.* local distortions and electron density distributions, but only the Coulomb interaction. In fact, for the $3 \times 3 \times 3$ supercell, the 1_{NN} Mn-V association is twice as large as the 1_{NN} Lu-V association in

agreement with their different charge states relative to the ideal lattice. The absolute value of the 1_{NN} Mn–V and Lu–V association energy is 27% larger than the corresponding Coulomb energy (−0.58 eV for Mn). However, the 2_{NN} Lu–V association energy is nearly zero and the absolute value of the 2_{NN} Mn–V association energy is 71% larger than the absolute value of the calculated Coulomb energy (−0.12 eV). Therefore, the above-stated assumption fails and the association energy is influenced by elastic contributions. Beyond that, the equivalent radii for Ce⁴⁺ and Lu³⁺ seem to affect the association energy as the 2_{NN} RE–V association energy has a maximum for Lu.

The strong association for Sc is in agreement with its low experimental solubility.^{64,118} Metropolis Monte Carlo calculations confirm phase separations for larger dopant fractions caused by formation of Sc–V associates.⁴⁶

The results of this work are compared with our earlier publications in detail in the Appendix: computational details.^{44,46} Comparison with these and other theoretical studies shows a strong influence of the used method, the supercell size and the termination at 3_{NN} on the association energy.^{36,37,41,138,142–145,147–151} As a result, both positive and negative RE–V association energies were reported and the transition between energy-favorable 1_{NN} and 2_{NN} interactions appears at different dopant radii. For example, Dholabhai *et al.* predicted an energy-favorable 2_{NN} Pr–V interaction at a dopant radius of 1.126 Å,^{145,147,148} while Andersson *et al.* and Nilsson *et al.* already found similar association energies for 1_{NN} and 2_{NN} Pm–V at a dopant radius of 1.093 Å.^{41,151}

The values for the ‘apparent association energy’ as discussed in Section 2.3 are defined as positive values and confirm a strong association of Sc doped ceria. Likewise, a stronger association of Y compared to Gd or La is measured. The range of calculated and experimental apparent association energies is similar. However, the smallest apparent association energy is measured for Gd, in contrast to the calculated 1_{NN} association energies. Though the experimental values scatter and earlier considerations also mention the possibility of extrapolating experimental values to infinitely low concentrations,⁴⁶ a significant difference between calculated 1_{NN} association energies and experimental apparent association energies is found. Consequently, a direct comparison of calculated 1_{NN} association energies with experiments might not be possible as *e.g.* for La doped ceria, oxygen vacancies are also trapped in the 2_{NN} position.

The values for the ‘apparent association energy’ as discussed in Section 2.3 are defined as positive values and confirm a strong association of Sc doped ceria. Likewise, a stronger association of Y compared to Gd or La is measured. The range of calculated and experimental apparent association energies is similar. However, the smallest apparent association energy is measured for Gd, in contrast to the calculated 1_{NN} association energies. Though the experimental values scatter and earlier considerations also mention the possibility of extrapolating experimental values to infinitely low concentrations,⁴⁶ a significant difference between calculated 1_{NN} association energies and experimental apparent association energies is found. Consequently, a direct comparison of calculated 1_{NN} association energies with experiments might not be possible as *e.g.* for La doped ceria, oxygen vacancies are also trapped in the 2_{NN} position.

The resulting influence of several RE–V and additional V–V interaction energies (see the next section) on the ionic conductivity can be properly compared with conductivity experiments by calculating the temperature-dependent ionic conductivity using Kinetic Monte Carlo (KMC) simulations (see Appendix: theoretical details and Kinetic Monte Carlo).

3.1.2 V–V repulsion energy. For the repulsive interaction of two oxygen vacancies, a fast decrease in the positive repulsion energy is found between the 1_{NN} and 2_{NN} interaction (Fig. 9). The further interactions are similar up to the 5_{NN} V–V interaction. For larger defect distances, the V–V interaction is small, *e.g.* below 0.02 eV between the 6_{NN} and 5_{NN} V–V interaction. Therefore, all V–V repulsion energies are given relative to the 5_{NN} V–V interaction and larger defect distances will be neglected in

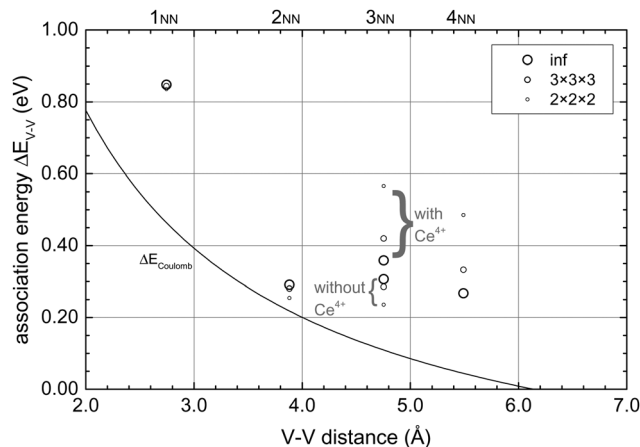


Fig. 9 V–V interaction energy as a function of the V–V distance. Different supercell sizes are calculated under the assumption of $\Delta E_{V-V}^5 = 0$ (see text). The line indicates the classical Coulomb energy, which is calculated for an ideal lattice geometry.

the following. For the 3_{NN} V–V interaction, there are two possible geometries for the space diagonal, one without (3_{NNa}) and one with a cation between the oxygen vacancies (3_{NNb}). Both show significantly different repulsion energies due to lattice relaxations caused by the cation between the oxygen vacancies, though the repulsion energy difference decreases with increasing supercell size.

The 1_{NN} V–V interaction energy is independent of the supercell size. For other V–V distances, increasing the supercell sizes leads to both lower and higher repulsion energies, probably due to different shielding effects of the surrounding cations.

The results are in agreement with Ismail *et al.*, who also found a rapid decrease in the V–V repulsion after the first shell, similar energies for 2_{NN} to 4_{NN} and a negligible 5_{NN} V–V interaction.¹⁵² The results are compared with our earlier publications in the Appendix: computational details.

3.1.3 High defect concentrations. Until now, only the interaction of two defects was investigated. Now, a pair interaction model is assumed for the configuration energy of the lattice where interaction energies of multiple defects are just summed up and thus linearly scaled. Therefore, the lattice configuration energy E_{conf} can be calculated with the number of interactions N_i and the distance i based on DFT calculations of the RE–RE, RE–V and V–V interaction energies E_i :

$$E_{\text{conf}} = \sum_i N_{\text{RE-RE},i} \cdot E_{\text{RE-RE},i} + \sum_i N_{\text{RE-V},i} \cdot E_{\text{RE-V},i} + \sum_i N_{\text{V-V},i} \cdot E_{\text{V-V},i} \quad (3)$$

DFT calculations of a $3 \times 3 \times 3$ supercell with two Sm dopants and one oxygen vacancy, in accordance with eqn (1), confirm the validity of the pair interaction model as already found in an earlier work from 2009.⁴⁴ The energy differences between the 1_{NN} and either the 2_{NN}, 4_{NN} or 5_{NN} Sm–V interaction nearly double for an additional Sm dopant, which is introduced at the same interaction distance to the oxygen vacancy, with deviations less than 0.005 eV.

For higher defect concentrations that are similar to dopant fractions in experimentally used materials, Metropolis Monte Carlo simulations in a $3 \times 3 \times 3$ supercell were performed according to an earlier work⁴⁶ to equilibrate the positions of cations and anions at 1500 K and subsequently only the anion positions at 900 K similar to the experimental sintering process for $\text{Ce}_{1-x}\text{Sm}_x\text{O}_{2-x/2}$ with $x = 0.05, 0.1$ and 0.15 . Subsequently, the energy of the supercell was determined using DFT calculations in the same supercell. In this work, the influence of the lattice configuration energy on the oxygen migration is of special interest. Therefore, typical jump configurations were identified and jumps were performed using again DFT calculations. The difference between the initial and the final state of an oxygen ion jump (e.g. illustrated in Fig. 6) gives a lattice configuration or interaction energy difference, which is crucial to the investigation of diffusion in doped ceria. The DFT interaction energy differences were compared with the lattice configuration energy differences according to eqn (3). For eqn (3), the calculated interaction energies for infinitely dilute defects were used. This comparison helps to validate both the use of the pair interaction model and the used interaction energies.

In total, 450 interaction energy differences were investigated. It should be noted that the DFT calculations now include RE-V and V-V interactions simultaneously. Fig. 10 shows a good agreement between model lattice configuration and DFT interaction energy differences, especially for low defect concentrations. With increasing dopant fractions, the standard deviation σ_s increases to 0.09, 0.12 and 0.15 for $x = 0.05, 0.1$ and 0.15 , respectively. Considering all dopant fractions, σ_s is 0.13. The good agreement validates that a pair interaction model with independent RE-V and V-V interactions can be used for the lattice configuration energy.

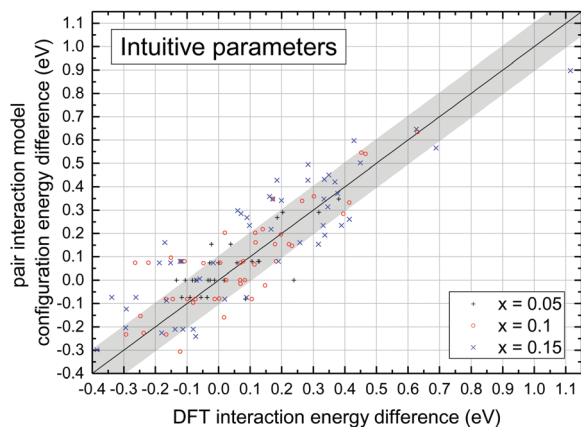


Fig. 10 Model configuration and DFT interaction energies with intuitive parameters as discussed in Section 3.3. $\text{Ce}_{1-x}\text{Sm}_x\text{O}_{2-x/2}$ in a $3 \times 3 \times 3$ supercell. The migrating oxygen vacancy interacts with both dopants and vacancies. The DFT calculations include simultaneous RE-V and V-V interactions. Association energies around the migrating oxygen vacancy up to 2_{NN} RE-V and 4_{NN} V-V (5.41 Å) are added up. Intuitive parameters are chosen for the extrapolated supercell with the termination $E_{\text{ass}}(3_{\text{NN}} \text{RE-V}) = 0$ and $E_{\text{ass}}(5_{\text{NN}} \text{V-V}) = 0$. The line identifies identical model and DFT results, and the gray area shows an error of 0.1 eV.

3.2 Blocking: migration edge

Fig. 11 shows migration energies in pure and diluted rare-earth doped ceria of different supercell sizes at constant volume, which is given by the relaxed defect-free bulk material at zero temperature.¶ Three selected geometrically symmetric jump configurations are shown: the Ce-Ce, Ce-RE and RE-RE edge (cf. Fig. 2).

For each rare-earth dopant, the migration edge energy for the RE-RE edge is larger than for the Ce-RE edge. A minor exception is only the $2 \times 2 \times 2$ supercell of Sc doped ceria, probably due to a too small supercell size. Doped edges can have lower migration energies than pure ceria, e.g. for Sc, Mn and Lu doped ceria. For large dopants at the migration edge, the migration of oxygen ions is blocked. The migration edge energies for Ce-RE and RE-RE edges increase with increasing dopant size. The unusual behavior of Yb doped ceria may be a result of the PAW-PBE potential (see Appendix: computational details) used in the Vienna *Ab initio* Simulation Package (VASP) for Yb, which was originally optimized for Yb^{2+} . Generally, a nearly linear behavior between migration edge energy and dopant radius is found.

The migration energy for an infinitely large supercell ('inf') was calculated according to Makov and Payne (see Appendix: computational details) using the $2 \times 2 \times 2$, $3 \times 3 \times 3$ and $4 \times 4 \times 4$ supercells. We found that it is sufficient to use only the $2 \times 2 \times 2$ and $3 \times 3 \times 3$ supercells (Fig. 11) as the extrapolated result is similar. The supercell size determines the distance between the migrating oxygen vacancy and its mirror image,

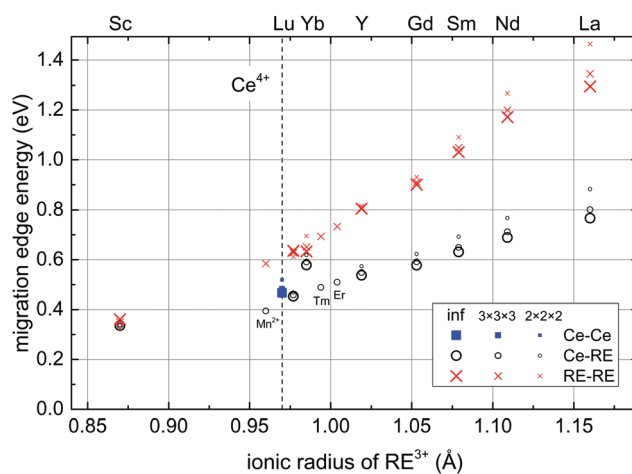


Fig. 11 Migration energy as a function of the ionic radius of RE^{3+} of the Ce-Ce, Ce-RE and RE-RE edge (cf. Fig. 2). Different supercell sizes are calculated.

¶ Relaxing the volume of supercells, which are containing defects, would lead to different lattice parameters. Calculations could be performed at constant pressure, i.e. the volume would be relaxed during the migration. This would lead to a change in the volume of both initial and transition states. However, the change in volume during the jump of the oxygen ion is limited as atomic displacements in a solid proceed with the speed of sound. Therefore, calculations of the constant volume case are used in the following.

i.e. its copy due to the applied periodic boundary conditions. The change in migration energy with increasing cubic supercell size is negative for large dopants (*e.g.* La), positive for small dopants (Sc) and negligible for Lu, which has a similar ionic radius as Ce^{4+} , mainly due to lattice relaxation effects.

Correlations between the migration edge energy and the atom coordinates show that the migration energies of the edge configurations change linearly with the widening of the edge cations.¹⁰⁸ The widening is the difference of distances of the edge cations in the transition state and the initial state. Simply described, this means that the cations at the edge must be pushed apart during the jump.

Additionally, the dopants Mn^{2+} , Tm^{3+} and Er^{3+} are shown as they have migration energies similar to pure ceria. Mn^{2+} shows a similar behavior of the migration edge energy as a function of ionic radius as the RE^{3+} dopants though it has a different charge state. This is contrary to the Coulomb-like behavior of the Mn–V association energy (see Fig. 8) and suggests that the migration energy is rather a function of the widening of the edge cation while the association energy is dominated by the Coulomb energy.

Comparing the supercell size dependencies of the migration energy (Fig. 11) and the association energy (Fig. 8) is surprising. For La doped ceria, the migration energy decreases with increasing cubic supercell size while the association energy increases. As both energies feature an opposite sign, the absolute value of both energies decreases with increasing cubic supercell size for La doped ceria (*cf.* Fig. S3, ESI[†]), *i.e.* both energies are overestimated in small supercells. The supercell size dependence changes for smaller dopants: for the Ce–Lu and Lu–Lu edge, the migration energy is independent of supercell size. For Nd doped ceria, the association energy is independent of supercell size. For the small dopant Sc, the absolute value of the migration and association energy increases with increasing cubic supercell size.

The results are in agreement with the literature: the migration energy increases with an increasing number of large dopants at the migration edge for Y,³⁸ La¹⁵³ or other dopants as shown in our earlier works.^{44,46} Additionally, we found an increase in migration energy with increasing dopant radius for doped migration edges.⁴⁴ Further literature results support this trend: for the Ce–RE edge, Dholabhai *et al.* found an increase in migration energy with increasing dopant radius of the dopants Gd (0.59 eV),¹⁴⁷ Sm (0.66 eV)¹⁴⁵ and Pr (0.78 eV).¹⁴⁸ For the RE–RE edge, Yoshida *et al.* found an increase in migration energy with increasing dopant radius for Y, Sm and La doped ceria.¹⁴² Andersson *et al.* confirmed this trend for several dopants.⁴¹

3.3 Model of the migration energy

3.3.1 Definition of the model. In doped ceria, numerous arrangements of cerium ions, dopants, oxygen ions and oxygen vacancies are possible around the migrating oxygen ion. The activation energies of oxygen migration in these numerous ionic configurations can be predicted by creating a model for the migration energy. In this regard, the lattice sites, whose occupation influences the migration energy, have to be identified and their influence has to be quantified.

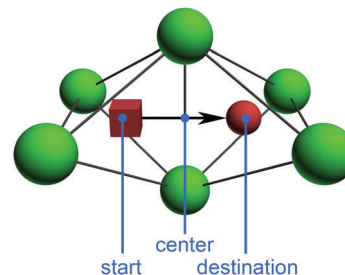


Fig. 12 Centers of interaction for oxygen migration in rare-earth doped ceria. The positions of the migrating oxygen vacancy are given: start (s), center (c) and destination (d). For colours, see Fig. 2.

According to Coulomb's law, forces between charged particles depend on their distance. Therefore, lattice sites in a sphere around the migrating oxygen ion are tested for their influence on the migration energy. The radius of the sphere is called interaction radius. Since the migrating oxygen ion changes its position during a jump, the interaction sphere can be expanded around the oxygen ion in the initial state, the transition state and the final state. As defects are easier to track, interactions are labeled in accordance with the position of the migrating oxygen vacancy in the start (s), center (c) or destination position (d) as shown in Fig. 12.

On each lattice site of rare-earth doped ceria either a host ion (Ce, O) or a defect (RE, V) is positioned. For each lattice position, which is considered in the calculation of the migration energy besides the positions of the migrating oxygen, the number of jump configurations multiplies by 2. This leads to a total number of 2^n jump configurations for n influencing positions, where some jump configurations are symmetrically equivalent. For example, for Fig. 12, up to 2^6 jump configurations are possible. Furthermore, including the next anion shell around the start and destination position would lead to 2^{16} jump configurations.

If not every configuration can be calculated, the approximation could be formulated that the influence of each lattice site is independent of the occupation of all other lattice sites. For every lattice site, the change in migration energy could be quantified in case a defect (RE, V) is present. This follows a pair interaction model, which has already been successfully applied above for the lattice configuration energy. Lattice sites featuring the same change in migration energy could be grouped according to their distance i to the start, center or destination position p of the oxygen vacancy during the jump. Then, the migration energy can be calculated according to

$$E_{\text{mig}} = E_{\text{mig,pure}} + \sum_{p,i} \varepsilon_{\text{shell},p,i}, \quad (4)$$

where $E_{\text{mig,pure}}$ is the migration energy in the pure material, where no RE–V and V–V interactions are present, and $\varepsilon_{\text{shell},p,i}$ gives the change in migration energy caused by each group.

The migration energy can either change linearly for increasing number of defects $N_{\text{shell},p,i}$ on lattice sites of the group p,i :

$$\varepsilon_{\text{shell},p,i}^{\text{lin}} = N_{\text{shell},p,i} E_{\text{shell},p,i}, \quad (5)$$

where $E_{\text{shell},p,i}$ is the energy change per defect of the migration energy. This is called *linear* scaling. If all ions were fixed at the positions of the ideal lattice, Coulomb's law would suggest that all lattice sites with the same distance to the migrating oxygen ion can be grouped with linear scaling.

However, in reality, a displacement of ions (relaxation) takes place. Therefore, the influence of individual lattice sites can depend on other lattice sites. This is, for example, the case when multiple defects form a cluster, which influences the migration energy differently than the sum of the separate defects. Nevertheless, the migration energy can still be modeled if lattice sites can be grouped and the change in migration energy depends on the total number of defects in the group. The change is not proportional to the number of defects but for every number of defects a change in migration energy is defined, e.g. for a group with two lattice sites the migration energy contribution is

$$e_{\text{shell},p,i}^{\text{cat}} = \begin{cases} 0 & \text{for 0 defects} \\ E_{\text{shell},p,i}^1 & \text{for 1 defect} \\ E_{\text{shell},p,i}^2 & \text{for 2 defects} \end{cases} \quad (6)$$

This is called *categorical* scaling.

For a better understanding, the migration energy changes can be classified as symmetric and asymmetric contributions (Fig. 13). *Symmetric* influences are characterized by changes in the migration energy, which are independent of the jump direction. If the presence of a defect changes the migration energy identically for forward and backward jumps, the resulting energy contribution is symmetric (blocking). Configurations that are geometrically symmetric around the jump center feature symmetric influences.

If the change in migration energy due to doping is different for the forward and backward jump of a specific ionic configuration, asymmetric energy contributions exist. Geometrically asymmetric configurations with defects near the start or destination position are often influenced by both *asymmetric* (trapping) and symmetric (blocking) contributions to the migration energy.

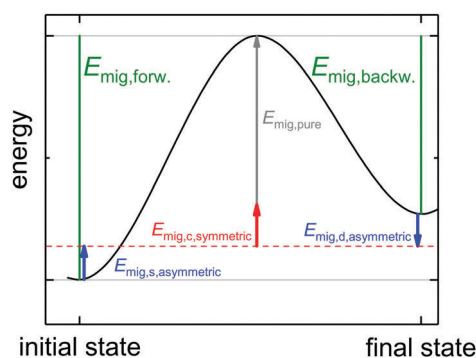


Fig. 13 Migration energy model predicting forward ($E_{\text{mig,forw.}}$) and backward jumps ($E_{\text{mig,backw.}}$) using symmetric ($E_{\text{mig,symmetric}}$) and asymmetric contributions ($E_{\text{mig,asymmetric}}$). $E_{\text{mig,pure}}$ is the migration energy in the pure material.

Furthermore, it is possible to combine groups near the start and destination position if their influence on the migration energy is exactly the opposite of each other. For example, if groups near the start and destination position scale linearly and their energy parameters are related according to $E_{\text{shell},d,i} = -E_{\text{shell},s,i}$ both groups can be combined:

$$\epsilon_{\text{shell},ds,i}^{\text{lin}} = (N_{\text{shell},d,i} - N_{\text{shell},s,i})E_{\text{shell},d,i} \quad (7)$$

The latter can be visualized by a linear interpolation between the energies of the initial and final state (cf. Fig. 13 for $E_{\text{mig},s,\text{asymmetric}} = -E_{\text{mig},d,\text{asymmetric}}$), which is common in the literature.^{154,155} Alternatively, a polynomial function for a better emulation of the assumed Coulomb potential between defects or sinusoidal shaped migration barriers can be introduced.¹⁵⁶ The migration energy difference between forward and backward jumps $E_{\text{mig,forw.}} - E_{\text{mig,backw.}} = \Delta E_{\text{conf}}$ is then given by the configurational energy difference between the final and initial state, which can be modeled according to eqn (3).

Finally, a model for the migration energy should predict the migration energies accurately with as few parameters as possible. Therefore, the interaction radius of the spheres around start and destination positions as well as the sphere around the center position should be reduced to a minimum. Possible interactions in doped ceria are shown in Fig. 14. A similar figure could be created for the destination position. The interaction radius should be chosen such that defects placed outside of the interaction radius have a negligible influence on the migration energy. As a first approximation, the above-discussed interaction radii of the RE-V and V-V interaction energies can be used.

For the nomenclature of the models, the following applies: a model that uses the first shell, which is centered at the jump center, is called “c1”. In doped ceria, a c1 model includes parameters for the Ce-Ce, Ce-RE and RE-RE edge. Further shells around the start, destination and center positions are numbered consecutively counting both cation and anion sublattices. For example, at the center positions, the models c1, c4, c5, c7 and c8 exist, while the 2nd, 3rd and 6th shells are

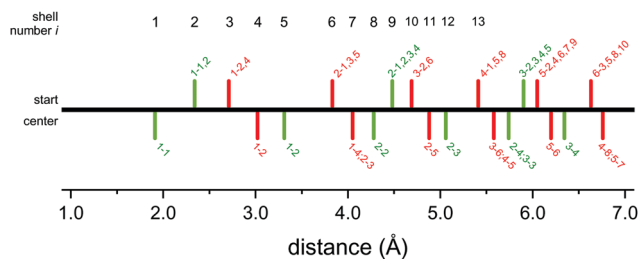


Fig. 14 List of RE-V (light green) and V-V interaction distances (red) of the migrating oxygen vacancy during a jump in doped ceria. Each interaction is represented by a bar. Bars are given as a function of the distance to the start position (up) or center position (down). However, interactions are labeled according to the distance of the defect to the oxygen vacancy before and after the jump. Therefore, bars with the same label can appear at different distances from the start position (up) and the center position (down). For example, “1–1,2” refers to 1_{NN} → 1_{NN} and 1_{NN} → 2_{NN} jumps, while “1–4;2–3” refers to 1_{NN} → 4_{NN} and 2_{NN} → 3_{NN} jumps.

centered at the start and destination positions. Alternatively, the interaction radius is directly given by the interaction distance. Here, distances are given according to the experimental lattice parameter of ceria at room temperature (5.41 Å).¹ Energy contributions using the difference between the number of defects between the destination and start position are called “sd [ds]”. From Fig. 13 it is obvious that these asymmetric contributions are connected in the linear approach with half of the change in energy between the initial and final state, which can be described as interaction energy difference. Energy contributions using the number of defects near the destination position and near the start position separately are called “sd [s,d]”.

The above-described approach to model the migration energy is often referred to as cluster expansion in the literature.^{154–158} Similar to this work, groups are formed according to space group symmetry of the crystal (asymmetric contributions for the configurational energy) and the highest coherent point group that maps the cluster onto itself (local cluster expansion). Often, groups scale linearly and the possibility of categorical scaling is neglected. Parameters are called effective cluster interactions and are often determined by a fit of several ionic configurations with several defects. Therefore, the scaling is possibly not systematically verified and insights into the parameters may be limited.

3.3.2 Classification of models used in the literature. In the literature, several models have been proposed to predict the migration energies in doped ceria or the isomorphic yttria-stabilized zirconia. Main differences are the interaction radii, the centers of interactions and the number of chosen parameters.

Krishnamurthy *et al.*¹⁵⁹ simulated the ionic conductivity in yttria-stabilized zirconia using an interaction radius of only 1.91 Å. They calculated the three edge configurations (c1) categorically: Zr–Zr, Zr–Y and Y–Y. The reduction of all possible migration energies to three values might be a bad approximation though we did not investigate yttria-stabilized zirconia in this work.

Meyer and Nicoloso¹³² included for fluorite-type oxides only the RE–V interaction and neglected any V–V repulsion. Separate models were created considering either trapping (sd [ds] with an interaction radius of 2.34 Å) or blocking (c1 categorically, where the migration edge configurations with one and two dopants have the same migration energy $E_{\text{shell},c1}^1 = E_{\text{shell},c1}^2$). In summary, trapping and blocking are only considered separately, the c1 model is badly approximated and no V–V repulsion is considered. Therefore, several effects are missing that are shown in this work to be essential to understand the ionic conductivity.

Adler and Smith¹⁶⁰ simulated the ionic conductivity in Y doped ceria. For the RE–V and V–V interaction, a modified Coulomb potential was used that contains an empirical scaling term that adjusts the range of the interaction. The range of interaction was varied between 1_{NN} and infinity for RE–V and V–V. The migration barrier that is added to this interaction energy difference was assumed to be independent of the ionic environment according to spin–lattice measurements.¹⁶¹ This led to a sd [ds] model with an interaction radius between 2.71 Å and infinity. While the linear scaling for sd [ds] is a good

approximation as confirmed in this work, the neglected categorical scaling of the c1 model leads to strong deviations compared to calculated migration energies.

In publications from 2006,^{34,162} 2009⁴⁴ and 2012,⁴⁵ we chose the c1 model categorically. In the analytical approach of 2006 as well as in the publication from 2009, we additionally added the RE–V interaction around the start position (c1 + s) using a linear scaling with an interaction radius of 2.34 Å (2006) and 4.48 Å (2009). However, this model has two disadvantages: as shown in this work, the destination position (d) is crucial to model the migration energy. Furthermore, no V–V interactions were considered. In 2012, we also considered the first V–V interaction for Y and Sm doped ceria. The resulting c1 + s model with an interaction radius of 2.71 Å allows a clear separation of blocking and trapping effects. However, the model quality is limited (see discussion in the next section) as only a few parameters are used.

All configurations of the ‘6-cation environment’ (see Fig. 2) were calculated by Murray³⁸ and Oaks *et al.*¹⁵³ using empirical potentials for Y and La doped ceria, respectively, and by Pornprasertsuk *et al.*¹⁶³ using DFT for yttria-stabilized zirconia. The latter was also investigated by Shimojo and Okazaki¹⁶⁴ by extracting the jump configurations of performed jumps from molecular dynamics (MD) simulations. The resulting 30 parameter model (scd model without grouping and scaling) with an interaction radius of 2.34 Å is an acceptable approximation for the RE–V interaction of the migrating oxygen vacancy. However, no V–V repulsion was considered leading to unphysical results for high dopant fractions. In a later model, Pornprasertsuk *et al.*¹⁶⁵ increased the interaction radius to include 2_{NN} RE–V and V–V interactions using linear scaling.

A larger interaction radius was considered by Dholabhai *et al.*^{145,166–168} for Pr, Gd and Sm doped and Gd–Pr co-doped ceria. For the RE–V interactions, migration energies with a single dopant up to a 3_{NN} RE–V distance were calculated. Though the exact formula for the model is not mentioned, the created model could be similar to a c1 + c8 + c15 + sd [s,d] model with linear scaling, where the 1st, 8th and 15th shells around the center (c) counting both cation and anion sublattices are included, and an interaction radius of 4.48 Å is used considering only the cation sublattice. A first model without V–V interactions and a second model prohibiting vacancies from being on the 1_{NN} V–V position were used. As the c1 model is not calculated categorically and barely any V–V interactions are considered, large deviations between model and actual migration energies at high dopant fractions are expected.

Using a cluster expansion, Lee *et al.*¹⁵⁶ fitted 100 randomly chosen ionic configurations in yttria-stabilized zirconia with an interaction radius that is 50% larger than the lattice parameter. Though the model with 9 parameters has a good fit quality, insights into the significance of the parameters are limited.

In an earlier presented work from 2014,⁴⁶ we simulated the ionic conductivity in Y doped ceria using a c1 + sd [ds] model with categorical scaling for the c1 model and linear scaling for the sd model and an interaction radius of 4.69 Å. The model has a high quality as discussed in the next section. Deviations

from this work are discussed in the Appendix: computational details.

3.3.3 Quality of different models. In this section, an overview of the quality of different models is given using DFT calculations. Firstly, we calculate cells containing the migrating oxygen vacancy and either dopants or additional oxygen vacancies. Secondly, cells that include simultaneous RE–V and V–V interactions are calculated, where the jumping oxygen vacancy interacts with both dopants and vacancies. The DFT calculations include dopants and oxygen vacancies with different interaction distances and different concentrations. The quality of different models is determined by fitting a model to several migration energies obtained from DFT calculations. The quality of the fit is evaluated using the adjusted coefficient of determination \bar{R}^2 and the residual standard error σ_{residual} . For a perfect fit, \bar{R}^2 should be 1 and σ_{residual} should be 0.

In Fig. 15, 396 migration energies of exemplary¹⁶⁹ jump configurations containing the migrating oxygen vacancy and either dopants or additional oxygen vacancies for Sm doped ceria in a $3 \times 3 \times 3$ supercell were fitted using different models. For all models, the migration edge (c1) is considered categorical. Defect distances up to 6.76 Å are included. \bar{R}^2 and the residual standard error for different models show an improvement for most models with increasing interaction radius.

Clearly, models using only spheres around either the start (s), the center (c) or the destination position (d) are not sufficient to describe the migration energies of the 396 chosen jump configurations (Fig. 15). Even a combination of spheres at start and center (sc), which is similar to the approach of the transition state theory, could only be used at large interaction radii. However, a combination of spheres at destination and center (cd) gives even better results at low interaction radii than spheres at all three positions using the difference of the number of defects between the start and the destination position (scd [ds]). Obviously, for Sm doped ceria, influences

around the destination position are strong as seen by the scaling of e.g. the $1_{\text{NN}} \leftrightarrow 2_{\text{NN}}$ and $2_{\text{NN}} \leftrightarrow 4_{\text{NN}}$ RE–V jumps.¹⁶⁹ Therefore, a migration energy model should include interactions of the migrating oxygen vacancy with defects around its position in the initial, transition and final state.

Using the largest number of parameters, as in the scd [s,d] model, and varying the interaction radius up to 6.76 Å not always leads to the largest adjusted \bar{R}^2 as the same regression quality can be reached with a lower number of parameters. At 6.76 Å, the scd [s,d] model reaches the highest adjusted \bar{R}^2 value for all models of 0.9804 and a residual standard error of 0.029. Here, 36 parameters are used. As the number of parameters is very large, a reduction of parameters is desirable. Without decreasing the quality of the model too much, the number of parameters can be decreased to 10 parameters in the model c1 + sd [ds] with an interaction radius of 5.41 Å and a resulting residual standard error of 0.077 and $\bar{R}^2 = 0.86$. Especially influences near the jump center can be reduced and therefore symmetric contributions neglected. As seen before, these are in most cases small compared to the asymmetric contributions.¹⁶⁹ A comparison between DFT and model energies for the model c1 + sd [ds] (5.41 Å) is shown in Fig. 16. An interaction radius of 5.41 Å corresponds exactly to the length of the unit cell. This is not surprising as the length of the unit cell correlates with the translation symmetry in the solid.

Another verification of the model c1 + sd [ds] (5.41 Å) is shown in Fig. 17 (left), where 244 migration energies of typical jump configurations containing oxygen vacancies and Sm dopants at typical experimental defect concentrations ($\text{Ce}_{1-x}\text{Sm}_x\text{O}_{2-x/2}$ with $x = 0.05, 0.1$ and 0.15) in a $3 \times 3 \times 3$ supercell were fitted using different models. Here, interactions between the cation and anion sublattice are included in the DFT calculations. Again, the c1 + sd [ds] model with an interaction radius of 5.41 Å has still a good quality to describe the migration energies. The adjusted $\bar{R}^2 = 0.80$ ($\sigma_s = 0.089$) is slightly lower compared to the separate investigation of the RE–V and V–V interactions as

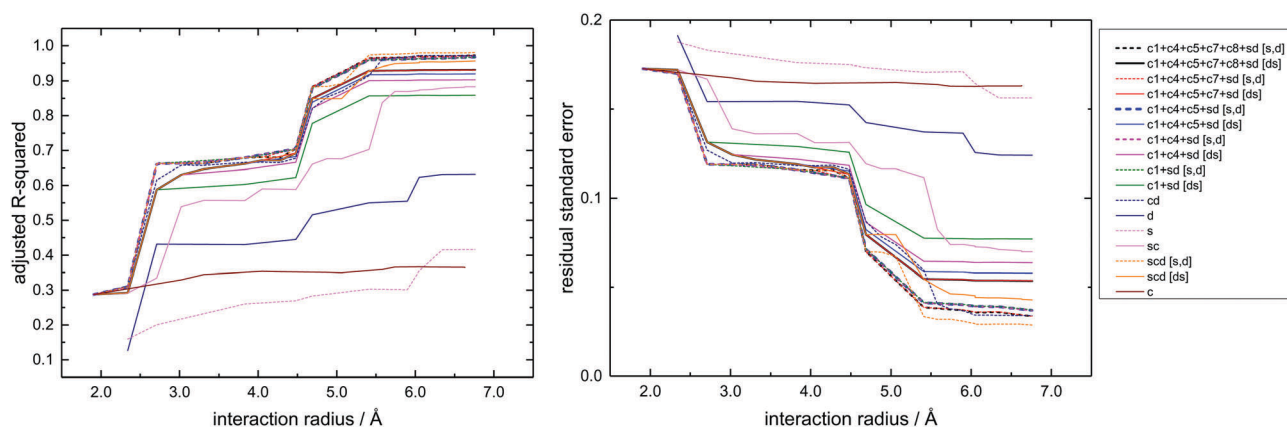


Fig. 15 Quality of the fit of migration energy models to DFT migration energies measured by \bar{R}^2 and standard deviation. The jumping oxygen vacancy interacts with either dopants or vacancies, i.e. the DFT calculations do not include simultaneous RE–V and V–V interactions. An interaction radius of up to 6.76 Å is included. For all models, the c1 part of the model is categorical. Either the given interaction radius (e.g. for the c model) or selected shells (e.g. for the c1 model) are used, where all shells around the start, destination and center positions are numbered consecutively counting both cation and anion sublattices. Sm doped ceria in a $3 \times 3 \times 3$ supercell.

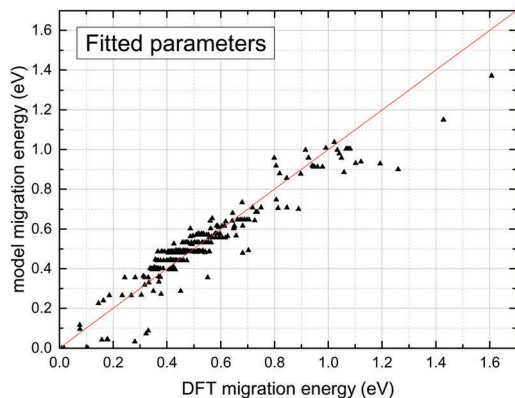


Fig. 16 Model and DFT migration energies with fitted parameters. The jumping oxygen vacancy interacts with *either* dopants or vacancies, *i.e.* the DFT calculations do not include simultaneous RE–V and V–V interactions. The model c1 + sd [ds] up to an interaction radius of 5.41 Å is used. Sm doped ceria in a 3 × 3 × 3 supercell.

discussed earlier. This is caused by the interaction of the ions and defects in the different sublattices and the larger defect concentration. The decrease in \bar{R}^2 is small, which indicates the following: the interaction between both sublattices is small and even migration energies at large defect concentration can be fitted using the proposed model.

Finally, the parameters of the model c1 + sd [ds] (5.41 Å) should be predicted rather than fitted to hundreds of configurations. The ability of the model c1 + sd [ds] to predict migration energies using intuitive parameters is shown in Fig. 17 (right). In this work, we chose intuitive parameters using the above-discussed RE–V and V–V interaction energies of the infinitely large supercell (Section 3.1) for the sd [ds] part of the model, which is linearly scaled. The sd [ds] part of the model (eqn (7)) can be visualized by a linear interpolation between the energies of the initial and final state (*cf.* Fig. 13

for $E_{\text{mig},s,\text{asymmetric}} = -E_{\text{mig},d,\text{asymmetric}}$). As discussed above, the terminations $E_{\text{ass}}(3\text{NN RE-V}) = 0$ and $E_{\text{ass}}(5\text{NN V-V}) = 0$ were used. The RE–V energy parameters (see Fig. 18) are defined, for example, according to $E_{\text{shell},d,2} = -E_{\text{shell},s,2} = -0.5 \cdot (E_{\text{RE-V},2} - E_{\text{RE-V},1}) + E_{\text{shell},d,9}$ and $E_{\text{shell},d,9} = -E_{\text{shell},s,9} = -0.5 \cdot (0 - E_{\text{RE-V},2})$. For the c1 part of the model, the Ce–Ce ($E_{\text{mig},\text{pure}}$), Ce–RE ($E_{\text{shell},c1}^1$) and RE–RE ($E_{\text{shell},c1}^2$) migration edge energies of the infinitely large supercell are used (Section 3.2).

In Fig. 17 (right), the standard deviation increases with increasing dopant fractions. For the intuitive parameters,

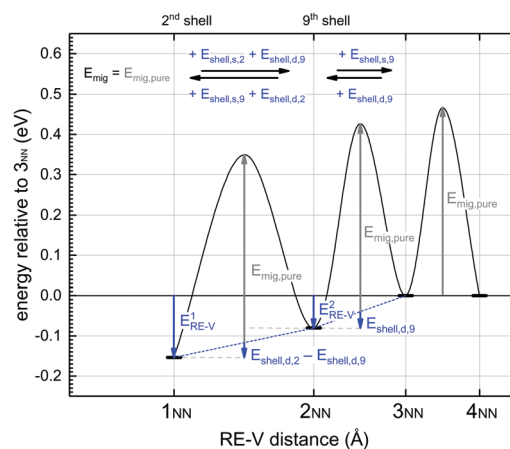


Fig. 18 Model migration energies (c1 + sd [ds], 5.41 Å) of the oxygen vacancy migration near a RE dopant. Only the RE–V association between one oxygen vacancy and one dopant is shown. Intuitive parameters are based on the RE–V association energies $E_{\text{RE-V},1}$ and $E_{\text{RE-V},2}$ (Fig. 8) with $E_{\text{RE-V},3} = 0$. The energy parameter for the 9th shell $E_{\text{shell},d,9}$ is directly given by the association energy difference, $E_{\text{shell},d,9} = -E_{\text{shell},s,9} = -0.5 \cdot (0 - E_{\text{RE-V},2})$. The energy parameter for the 2nd shell $E_{\text{shell},s,2}$ also depends on the parameter of the 9th shell as the 2NN RE–V distance is still included in the migration energy model. In this way, $E_{\text{shell},s,9}$ cancels out and the migration energy for a $1\text{NN} \rightarrow 2\text{NN}$ RE–V jump only depends on $E_{\text{RE-V},2} - E_{\text{RE-V},1}$. Energies are shown for Sm doped ceria in an infinitely large supercell.

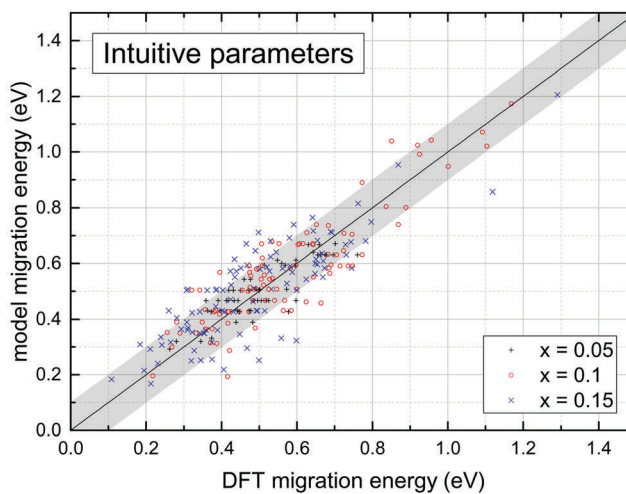
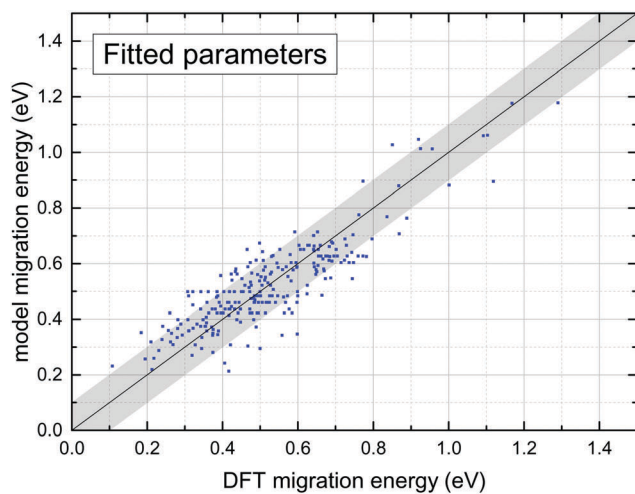


Fig. 17 Model and DFT migration energies with fitted and intuitive parameters. The jumping oxygen vacancy interacts with *both* dopants and vacancies. The DFT calculations include simultaneous RE–V and V–V interactions. The model c1 + sd [ds] up to an interaction radius of 5.41 Å is used. Intuitive parameters are chosen for the infinite supercell as discussed above with the terminations $E_{\text{ass}}(3\text{NN RE-V}) = 0$ and $E_{\text{ass}}(5\text{NN V-V}) = 0$. The line identifies identical model and DFT results; the gray area shows an error of 0.1 eV. Sm doped ceria in a 3 × 3 × 3 supercell.

σ_s is 0.06, 0.09 and 0.11 for $x = 0.05, 0.1$ and 0.15 , respectively. Including all dopant fractions leads to a σ_s of 0.093. The deviation from the regression of the fitted parameters is small. Therefore, the chosen intuitive parameters are well suited for experimental defect concentrations and are used for the Kinetic Monte Carlo simulations in the next section.

In summary, we defined a general model for the migration energy with a variable number of parameters. We calculated 640 migration energies using DFT calculations of exemplary jump configurations. Subsequently, we fitted models with different numbers of parameters to the calculated migration energies. Firstly, we only investigated jump configurations containing the migrating oxygen vacancy and either dopants or additional oxygen vacancies. Subsequently, we chose a model which fits well with the DFT migration energies and uses only a small number of parameters. Secondly, calculations with both oxygen vacancies and dopants at typical experimental defect concentrations were investigated. Both cases fit well for the selected migration energy model. As a result, our model based on pair interactions can be used to describe the DFT migration energies. Finally, we used the migration energies of only a few jump configurations to predict the parameters of our model. These parameters describe the DFT migration energies well. Furthermore, their effect on the migration energy can be easily understood and is intuitive.

4 Ionic conductivity

4.1 Simulation and experiments

Ionic conductivities for doped ceria with different rare-earth dopants were calculated using Kinetic Monte Carlo (KMC) simulations.¹⁷⁰ For this purpose, a random cation distribution was applied according to our earlier works (see Appendix: Kinetic Monte Carlo).^{46,108} The migration energy model $c1 + sd$ [ds] (5.41 Å with categorical scaling for the migration edge, $c1$, and linear scaling for the sd [ds] part of the model) was used for the KMC simulations. The applied intuitive parameters are discussed in the last paragraph. The used three migration edge energies are shown in Fig. 11 and the used six interaction energies are shown in Fig. 8 and 9. Changes in the migration energy compared to pure ceria can be classified as symmetric (blocking) and asymmetric contributions (trapping) as described in Section 3.3.

In Fig. 19, simulated ionic conductivities at 500 °C for Lu, Yb, Y, Gd, Sm, Nd and La doped ceria are compared. A contour plot of the data can be found in Fig. 20. The conductivity depends strongly on the temperature as shown in Fig. S4 (ESI†) for 267 °C and 600 °C. Here, 267 °C was chosen as a compromise between good experimental impedance measurements of the bulk conductivity at low temperature and short computation times of KMC simulations at high temperature. Error bars show the sample standard deviation σ_s of 10 simulations, which indicates the expected range for the next simulation. The error for the expected value of the conductivity is significantly smaller.

All calculated conductivities for ceria doped with different rare-earth dopants show the typical increase and decrease in

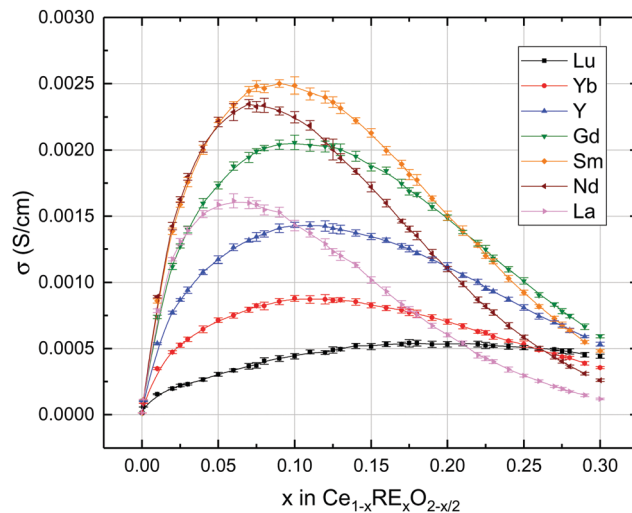


Fig. 19 Ionic conductivity of rare-earth doped ceria as a function of doping fraction. KMC simulations were performed at 500 °C with RE = Lu, Yb, Y, Gd, Sm, Nd and La. Lines are a guide to the eye only.

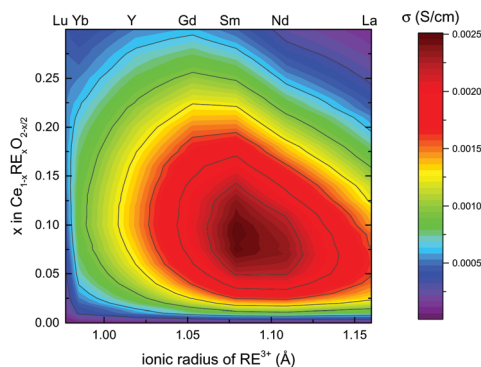


Fig. 20 Contour plot of the ionic conductivity of rare-earth doped ceria as a function of doping fraction. KMC simulations were performed at 500 °C with RE = Lu, Yb, Y, Gd, Sm, Nd and La.

ionic conductivity with increasing dopant fraction as found in experiments. The dopant fraction leading to the maximum in conductivity x_{\max} and the slope of the curves vary for different dopants. For most dopants, the characteristic maximum x_{\max} is around 0.1. An exception is Lu doped ceria due to its low migration edge energies as we will discuss in the next section.

The KMC simulations (Fig. 19) predict conductivities smaller by a factor of 0.3 than found in most experiments (Fig. 3). This may be caused by an underestimated attempt frequency or overestimated migration energies in the simulation. Alternatively, the separation of bulk and grain boundary conductivity in experiments may not be adequate. For impedance spectroscopy experiments, the bulk contributions often cannot be seen at 500 °C due to the limited measured frequency range but are extrapolated from measurements at lower temperature.

The highest conductivity in simulations is found for Sm doped ceria. In the experimental literature, the bulk conductivity was investigated only for a few dopant fractions. Therefore, impedance measurements were performed for a concentration

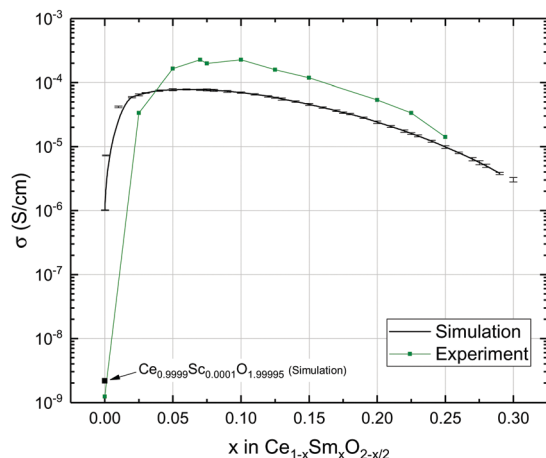


Fig. 21 Comparison of simulated and experimental ionic conductivity as a function of doping fraction. Sm doped ceria was investigated at 267 °C. Bulk ionic conductivities according to our impedance experiments are shown. Additionally, the simulated ionic conductivity of $\text{Ce}_{0.9999}\text{Sc}_{0.0001}\text{O}_{1.99995}$ is shown. Lines are a guide to the eye only.

series of Sm doped ceria in this work. Fig. 21 shows the simulated and experimental ionic conductivity of Sm doped ceria according to this work at 267 °C (for experimental details see Appendix: experimental details). A similar curve progression in simulations and experiments is found. Exceptions are found at small dopant fractions, where in the experiments impurities with high association energies influence the conductivity.¹⁰⁸ For example, Fig. 21 shows the simulated ionic conductivity for $\text{Ce}_{0.9999}\text{Sc}_{0.0001}\text{O}_{1.99995}$, which is significantly lower than the conductivities in Sm doped ceria and similar to the experimental conductivity of nominal pure ceria. We will present a detailed investigation of the effect of impurities on the ionic conductivity in our upcoming paper.¹⁷¹ The highest bulk conductivity is found for $\text{Ce}_{0.93}\text{Sm}_{0.07}\text{O}_{1.965}$ in experiments and for $\text{Ce}_{0.94}\text{Sm}_{0.06}\text{O}_{1.97}$ in simulations.

For different dopants, the ranking order for the highest conductivity is similar in simulations (Fig. 19) and experiments (Fig. 3) at different dopant fractions, despite the strong scattering in experiments: for low dopant fractions, Nd doped ceria often shows higher conductivities than Gd doped ceria. For large dopant fractions, this ranking order is reversed. Y doped ceria often shows lower conductivities than both dopants up to $x = 0.2$. Besides Gd and Nd doped ceria, Sm doped ceria possesses a large ionic conductivity. Dopants with smaller and larger ionic radii lead to lower maximal ionic conductivities. In the next section, a detailed comparison for $x = 0.1$ and 0.2 is performed.

The dopant fraction leading to the maximum in conductivity x_{max} for the simulation (Fig. 19) is in agreement with experiments (Table 1). Large dopants like Nd and La lead to small x_{max} in simulations and experiments.⁸⁶ Compared to previous KMC simulations in the literature, which predict too high x_{max} values, a better agreement with experiments is found in this work. For example, Dholabhai *et al.* predict at 500 °C a maximum for $\text{Ce}_{0.8}\text{Sm}_{0.2}\text{O}_{1.9}$ and at 400 °C a maximum for $\text{Ce}_{0.8}\text{Gd}_{0.2}\text{O}_{1.9}$.^{145,168} In our work from 2012, we predicted at 620 °C a maximum for

$\text{Ce}_{0.85}\text{Y}_{0.15}\text{O}_{1.925}$.⁴⁵ In our work from 2014, a maximum for $\text{Ce}_{0.86}\text{Y}_{0.14}\text{O}_{1.93}$ at 527 °C was predicted.⁴⁶ In both this work and experiments (Table 1) the dopant fractions leading to the maximum in conductivity are smaller. As a result, we predicted the ionic conductivity of rare-earth doped ceria better than previous KMC simulations that use energies from DFT calculations due to the improved migration energy model with improved parameters.

For 600 °C (Fig. S4, ESI†), all conductivities increase by a factor of about 2.5–4 compared to 500 °C (see also Inaba and Tagawa)²⁹ due to the Boltzmann probability. The increase in conductivity is higher for higher dopant fractions since the influence of blocking and trapping decreases with temperature. Though the (randomly ordered) cation configuration is independent of temperature, the number of jump attempts through Ce–Ce edges increases because the larger thermal energy increases the probability for oxygen vacancies to leave the association radius of the dopant ions (trapping). Furthermore, the probability of jumps through doped migration edges, which have a larger migration energy (blocking), is increased.⁴⁶ As a result, the maximum of the simulated ionic conductivity is shifted to larger dopant fractions, which is in agreement with experimental data (see Table 1 and Fig. S1, ESI†). Especially Y and Gd, which possess strong trapping, lead to high ionic conductivities at higher dopant fractions. At low temperature, the effects reverse and the dopant fractions leading to the maximum in conductivity decrease.

4.2 Volcano plots of the conductivity at $x = 0.1$ and 0.2

Similar to the literature, the ionic conductivity for a single dopant fraction can be investigated. Though often the total conductivity is presented in the literature, only the bulk conductivity represents the inherent property of the doped material largely without the influence of the microstructure of the sample. The bulk conductivity in experiments at 400 °C for $x = 0.1$ and 0.2 was summarized in Fig. 4 and is again shown in Fig. 22 (top).

For comparison, simulated ionic conductivities are shown in Fig. 22 (bottom). Here, the ionic conductivity increases with increasing dopant radius up to Sm and decreases with increasing dopant radius for larger dopants. For $x = 0.1$ and 0.2 , Sm is the optimal dopant with the highest conductivity as already shown in Fig. 19 and Fig. S4 (ESI†). The bulk conductivity in experiments is about a factor 2–4 ($x = 0.1$) or 2–6 ($x = 0.2$) larger than the simulated conductivity. An exception is Nd doped ceria, whose experimental values scatter over more than an order of magnitude. The ranking order between different dopants is similar in experiments and simulation.

In Fig. 22, a linear relationship between the ionic radius and the conductivity (solid lines) or the logarithm of the conductivity (dashed lines) is shown. If the conductivity depends linearly on the ionic radius, a relation between lattice distortions and the ionic conductivity can be assumed. If the logarithm of the conductivity depends linearly on the ionic radius, the ionic conductivity is dominated by the apparent activation enthalpy (according to $\sigma_i = \frac{A}{T} e^{-\frac{\Delta H_a}{k_B T}}$), which is strongly influenced by the

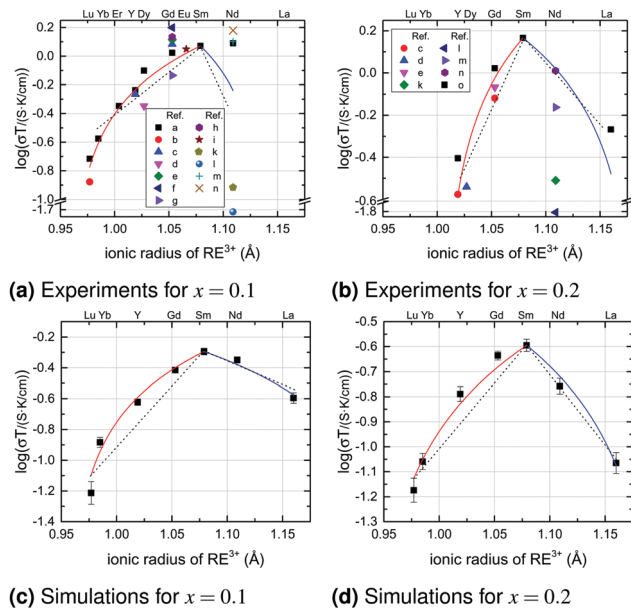


Fig. 22 Ionic conductivity of $\text{Ce}_{1-x}\text{RE}_x\text{O}_{2-x/2}$ at 400 °C for $x = 0.1$ and 0.2 according to experiments (top, cf. Fig. 4) and simulations (bottom). Experimental data from references a,⁸³ b,⁸² c,⁸⁵ d,⁶⁷ e,⁶¹ f,¹⁰⁶ g,⁹² h,⁹⁵ i,⁹⁶ k,⁷⁴ l,⁷³ m,¹⁰⁰ n¹⁰¹ and o⁸⁷ are shown. The lines show a linear relationship between the ionic radius and the conductivity (solid lines) or the logarithm of the conductivity (dashed lines).

ionic radius of the dopant. In fact, both relations were already reported in the literature as discussed in Section 2.5: first theories postulated that the highest oxygen ion conductivity occurs for dopants which result in the least distortion of the crystal lattice.^{1,28,30,31,84,133–136} Additionally, a relation between the activation enthalpy and the ionic conductivity was investigated.^{84,86,87,102,146}

The results in this work and literature suggest a linear relationship between ionic radius and conductivity in contrast to earlier literature as shown by the better regression result in Fig. 22.

4.3 Trapping and blocking

The ascending slope of $\sigma(x)$ as a function of the dopant fraction (Fig. 19) is small for small dopants (e.g. Lu, Yb and Y) and large for large dopants (e.g. La), obviously curve progression and ionic radius are related. This is not surprising, since the association energies (Section 3.1) and migration energies from density functional theory (DFT) calculations (Section 3.2), which were used in the KMC simulations, are related to the dopant radius. For further investigations, the input parameters and output values of the KMC simulations are categorized and compared.

Trapping and blocking are used to describe the experimental ionic conductivity as discussed in Section 2.4 and in theoretical studies.^{44–46} Trapping describes the influence of the association between dopant ions and oxygen vacancies on the migration energy. Migration barriers for jumps of the migrating oxygen vacancy away from the associating dopant are higher than in pure ceria, while jumps to the dopant are more favored.

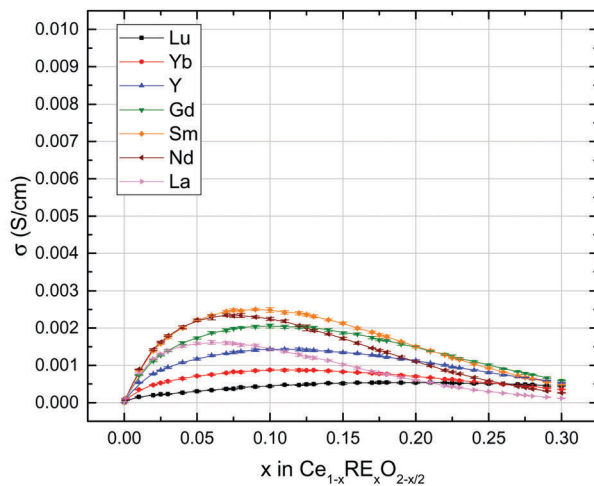
Vacancies appear more often in the nearest neighborhood to the defect because they are trapped. Blocking describes energy contributions that increase the migration energy for both the forward jump and the backward jump. Oxygen vacancies are kinetically hindered and therefore blocked. The trapping decreases for larger ionic radii (Fig. 8) while the blocking effect increases (Fig. 11).

To investigate the influence of blocking, trapping and the V–V interaction on the ionic conductivity, several simulations were performed. In these simulations, increased symmetric migration barriers due to dopants around the jump center (blocking) or association energy contributions due to the RE–V association (trapping) or V–V repulsion were neglected (Fig. S5, ESI[†]). For Sm doped ceria, it was found that with no V–V repulsion a strong association of dopants and vacancies takes place and the conductivity decreases. Therefore, the V–V repulsion increases the conductivity. Blocking and trapping both decrease the conductivity.

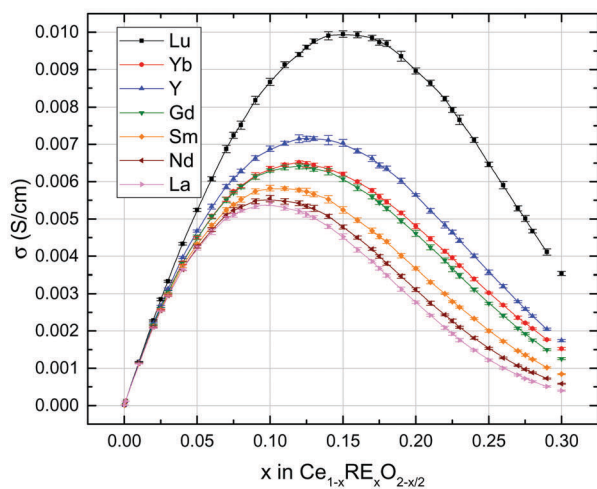
While these observations were made for Sm doped ceria, similar effects might be found for other rare-earth dopants. The V–V repulsion energies are independent of the dopant. Therefore, the investigation of blocking and trapping is the main goal of this work as they are the only factors that distinguish the conductivity of different rare-earth dopants. Both effects are essential for the understanding of the underlying mechanism that determines the magnitude of the oxygen ion conductivity and the optimal dopant concentration.

Therefore, KMC simulations at 500 °C were performed for different rare-earth dopants with all (Fig. 23a) or only selected interactions (Fig. 23). Either trapping (Fig. 23b) or blocking (Fig. 23c) was neglected. For the no-trapping case, the blocking effect can also be dopant-dependent only for the Ce–RE edge by setting the RE–RE edge energy for all dopants to the largest calculated value of 1.29 eV. In this case, dopants differ only by the Ce–RE edge energy (Fig. 23d). For the no-blocking case, the trapping effects can also be restricted to a 1_{NN} RE–V interaction range by terminating at the 2_{NN} RE–V interaction. In this case, dopants differ only by the asymmetric energy contribution to the $1_{\text{NN}} \leftrightarrow 2_{\text{NN}}$ RE–V jump (Fig. 23e).

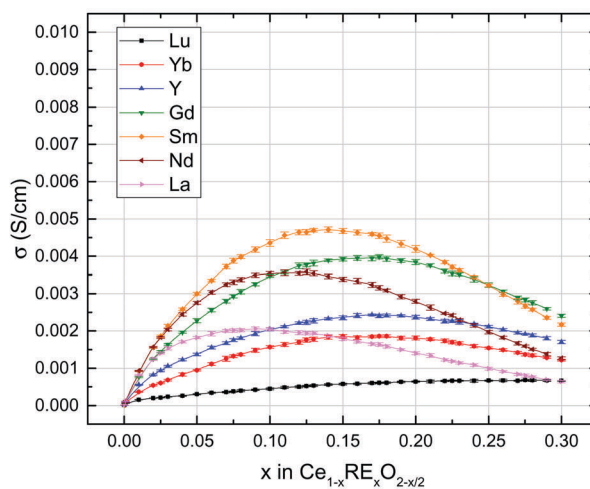
KMC simulations *with* (Fig. 23a) and *without trapping* (Fig. 23b) show the same ranking order of x_{max} between different rare-earth doped ceria. For Gd doped ceria, no change in x_{max} is found. Small dopants have lower x_{max} and large dopants have higher x_{max} if the trapping is included with a difference up to $\Delta x_{\text{max}} = \pm 0.04$. If, in addition to the trapping, the blocking effect is also modified and dopants differ only by the Ce–RE edge energy (Fig. 23d), hardly any change in the conductivity is found. An exception is Yb doped ceria, which has an exceptionally high Ce–RE edge energy that is similar to the Ce–Gd edge energy (Fig. 11), probably caused by the chosen PAW–GGA–PBE potential. A comparison between the Ce–RE edge energy and the dopant fraction of the maximum in conductivity is shown in Fig. 24 (left). The dopant fraction of the maximum decreases with larger blocking: for higher dopant fractions, the fraction of jump configurations influenced by blocking increases. Larger blocking leads to lower conductivities and, therefore, with larger blocking



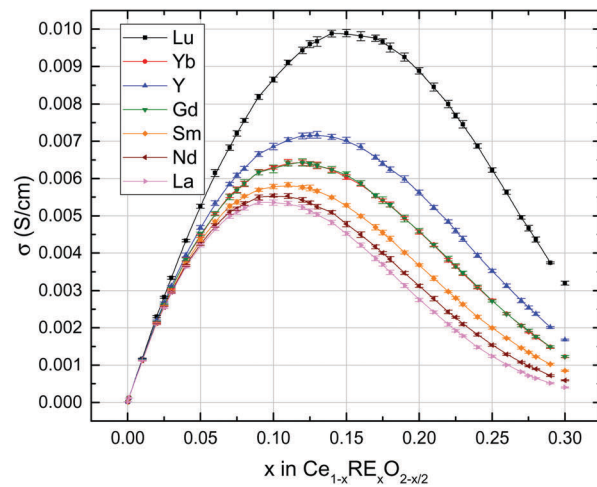
(a) all interactions



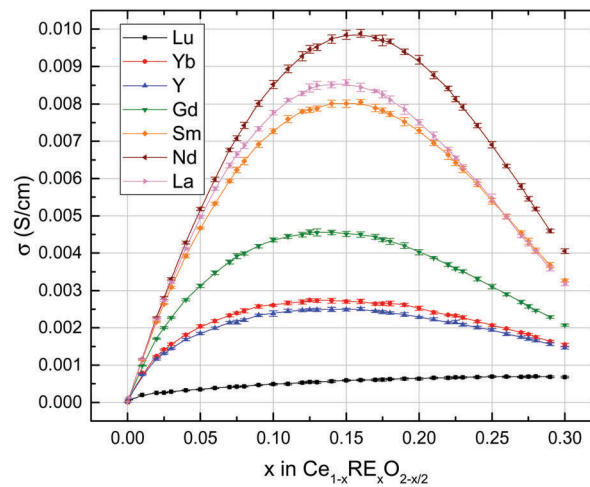
(b) no trapping



(c) no blocking



(d) only different Ce-RE edge



(e) only different $1_{NN} \leftrightarrow 2_{NN}$ RE-V jump

Fig. 23 Simulated ionic conductivity of rare-earth doped ceria at 500 °C without considering RE–V interactions around the start and destination position (left) or without considering different migration edges (right). Lines are a guide to the eye only.

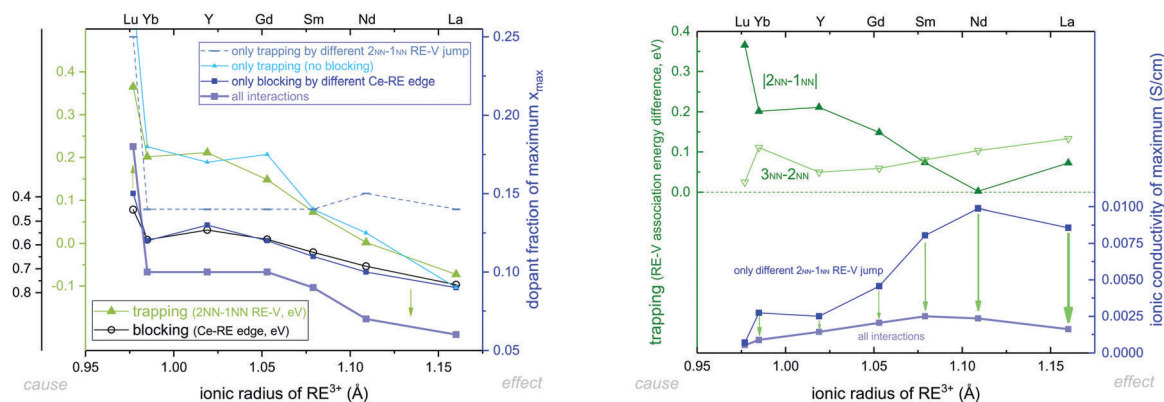


Fig. 24 Relationship between blocking and trapping and the simulated ionic conductivity for different dopants at 500 °C. A comparison between the Ce–RE migration edge energy (blocking) and the dopant fraction of the maximum (left) or the RE–V association energy difference (trapping) and the ionic conductivity of the maximum (right) is shown. For comparison, interactions are switched off individually. Lines are a guide to the eye only.

the maximum appears at lower dopant fractions. Hence, x_{\max} is determined by the Ce–RE edge energy.

However, the number of jumps through doped edges does not change much for larger dopant and vacancy fractions. In KMC simulations of an earlier work at 700 K, between $x = 0.02$ and 0.14 the relative number of jumps through Ce–Y edges increases only about 4% (35% to 39%).⁴⁶ Jumps through Y–Y edges are rare (0.04% to 0.14%). Significantly higher are the number of jump attempts, which are not weighted by the Boltzmann probability $p = e^{-\frac{\Delta E_{\text{mig}}}{k_B T}}$ (cf. Appendix: Kinetic Monte Carlo), with 45% to 54% (Ce–Y) and 2% to 11% (Y–Y). The large migration energy of doped edges decreases the number of performed jumps and therefore the ionic conductivity.

The ionic conductivity of the no-trapping case using only different Ce–RE edge energies is high compared to KMC simulations with trapping. The ranking order of the conductivities at all dopant fractions is equivalent to the ranking order of the Ce–RE edge energies. The ionic conductivity decreases with increasing Ce–RE migration edge energy or rather increasing dopant radius with the above-discussed exception of Yb doped ceria. Therefore, we can summarize: blocking mainly limits the dopant fraction of the maximum. Here, the Ce–RE edge energy is decisive.

KMC simulations at 500 °C *with* (Fig. 23a) and *without blocking* (Fig. 23c) show nearly the same ranking order of conductivities at all dopant fractions. If the trapping effect is also restricted and dopants differ only by the asymmetric contribution to the $1_{\text{NN}} \leftrightarrow 2_{\text{NN}}$ RE–V jump (Fig. 23e), the ranking order of conductivities changes significantly and is equivalent to the ranking order of the absolute value of the $|2_{\text{NN}}-1_{\text{NN}}|$ RE–V association energy differences (Fig. 8). A comparison between association energy differences and ionic conductivity of the maximum is shown in Fig. 24 (right). The ionic conductivity decreases with increasing absolute value of the $|2_{\text{NN}}-1_{\text{NN}}|$ RE–V association energy difference or rather increasing dopant radius. Sm and La doped ceria have similar conductivities though in Sm doped ceria the 1_{NN} RE–V association and in La doped ceria the 2_{NN} RE–V association are favored. Large $|2_{\text{NN}}-1_{\text{NN}}|$ RE–V association energy differences lead to steep slopes. If again

the full trapping effect is considered and therefore $2_{\text{NN}} \rightarrow 3_{\text{NN}}$, $2_{\text{NN}} \rightarrow 4_{\text{NN}}$ and $4_{\text{NN}} \rightarrow 4_{\text{NN}}$ RE–V jumps have different migration energies, the conductivities decrease with increasing 2_{NN} RE–V association energy or rather $|3_{\text{NN}}-2_{\text{NN}}|$ RE–V association energy difference. The decrease occurs especially at large dopant fractions if the $|2_{\text{NN}}-1_{\text{NN}}|$ RE–V association energy difference is small. The decrease occurs especially at small dopant fractions if the $|2_{\text{NN}}-1_{\text{NN}}|$ RE–V association energy difference is large. In other words, if the conductivity in Fig. 23e is high, the conductivity in Fig. 23c is smaller, especially at large dopant fractions. For intermediate 2_{NN} RE–V association energies, even an increase in conductivity at large dopant fractions can be found. This results in crossings in the ranking order of conductivities. Hence, the ranking order of conductivities is determined by the $|2_{\text{NN}}-1_{\text{NN}}|$ and $|3_{\text{NN}}-2_{\text{NN}}|$ RE–V association energy differences.

The dopant fraction leading to the maximum in conductivity is similar for different dopants if only the $|2_{\text{NN}}-1_{\text{NN}}|$ RE–V association energy differences are considered (Fig. 24 left). An exception is Lu doped ceria due to strong trapping. But, including the $|3_{\text{NN}}-2_{\text{NN}}|$ RE–V association energy differences increases x_{\max} for large $2_{\text{NN}}-1_{\text{NN}}$ RE–V association energy differences and decreases x_{\max} for negligible or negative $2_{\text{NN}}-1_{\text{NN}}$ RE–V association energy differences compared to the previous case. Here, Sm and La doped ceria show different behavior. This is shown in Fig. 24 (left). Surprisingly, the change in x_{\max} is independent of the $3_{\text{NN}}-2_{\text{NN}}$ RE–V association energy difference. We conclude: the dopant fraction leading to the maximum in conductivity is only directly controlled by the formation of RE–V associates if vacancies are already slowed down in the vicinity of the dopant due to the 2_{NN} association energy.

Though the resulting ranking order of x_{\max} between different rare-earth doped ceria for the no-blocking case is similar to the KMC simulations with all interactions, the values of x_{\max} are too large. Fig. 24 (left) shows the dopant fraction of the maximum if only blocking is considered. Large $2_{\text{NN}}-1_{\text{NN}}$ RE–V association energy differences increase and small $2_{\text{NN}}-1_{\text{NN}}$ RE–V association energy differences decrease x_{\max} . In summary, the dopant fraction leading to the maximum in conductivity is influenced by both trapping and blocking, but dominated by blocking.

We conclude: trapping mainly limits the maximum ionic conductivity value. Here, the association energy differences are decisive.

In summary, both trapping and blocking decrease the conductivity. However, to reproduce the correct ranking order of conductivities it is necessary to include trapping. The dopant fraction of the maximum x_{max} is limited by blocking. In the literature, the common assumption is made that association between oxygen vacancies and dopants causes the maximum in oxygen ion conductivity (Section 2.4). On the one hand, the result of this work indeed shows that trapping creates the ranking order of conductivities between different dopants and even has an influence on x_{max} . On the other hand, this work shows that the dopant fraction leading to the maximum in conductivity is limited by blocking. The optimal dopant fraction or optimal doping concentration cannot be predicted based on trapping alone. This defies the assumption in the literature and, therefore, blocking is strongly underrated in the literature.

The highest conductivity can be found if the absolute values of the association energy differences are small. The $2_{\text{NN}} \leftrightarrow 1_{\text{NN}}$ RE-V association leads to the formation of associates (either at 1_{NN} or at 2_{NN}). As a result, vacancies are held by the dopants as their movement is hindered. The long-range $3_{\text{NN}} \rightarrow 2_{\text{NN}}$ RE-V association pulls vacancies into the vicinity of dopants. Both need to be small for a large ionic conductivity.

In summary, not only a low tendency for associate formation but also a low pull of vacancies into the vicinity of dopants is important for a large ionic conductivity. For this purpose, the $2_{\text{NN}} \leftrightarrow 1_{\text{NN}}$ associate formation can be described as a hold of the vacancy and the $3_{\text{NN}} \rightarrow 2_{\text{NN}}$ RE-V association as a catch of the vacancy, resulting in the term ‘catch-and-hold principle’. The catch-and-hold principle explains why Sm doped ceria with medium trapping energies has the largest maximum ionic conductivity.

4.4 Activation enthalpy

Macroscopic apparent activation enthalpies ΔH deduced from the KMC simulations between 500 °C and 600 °C in steps of

25 °C were calculated (Fig. 25) similar to experimental data according to $\sigma = \frac{A}{T} e^{-\frac{\Delta H_a}{k_B T}}$ (see Appendix: theoretical details). It should be noted that the input parameters for the KMC simulations like the migration energy model are independent of dopant fraction and temperature. No reduction of ceria was taken into account.

As shown in Fig. 25, the simulated apparent activation enthalpies at low dopant fractions are equal to the migration energy in pure ceria of about 0.47 eV for all dopants. Each activation enthalpy increases with increasing dopant fraction. This is caused by the interactions between defects that increase the migration energies. Contrary to some literature results,^{74,84,86,100} no minimum in the activation enthalpy can be found at low dopant fractions. Impurities with high association energies or reduction dominated conductivities can explain the higher apparent activation enthalpies in experiments at low dopant fractions as discussed in an earlier publication.¹⁰⁸ We will present a detailed investigation of the phenomenon of the minimum in the apparent activation enthalpy in our upcoming paper.¹⁷¹ We conclude: no minimum in the apparent activation enthalpy is necessary to reproduce the maximum in the ionic conductivity as a function of dopant fraction. Our simulations reproduce the maximum in the ionic conductivity (*cf.* eqn (8) in Appendix: theoretical details) using increasing apparent activation enthalpies with increasing dopant fraction (Fig. 25), an increasing charge carrier concentration with increasing dopant fraction and approximately constant apparent experimental attempt frequencies (Fig. 26).

Activation enthalpies in simulations are smaller than in experiments. A non-sufficient separation of bulk and grain boundary conductivity in experiments may lead to overall higher activation enthalpies. In simulations, large and small dopants have high activation enthalpies. Medium sized dopants that lead to high conductivities have low activation enthalpies (Sm and Nd). Similarly, the ranking of dopants at a specific

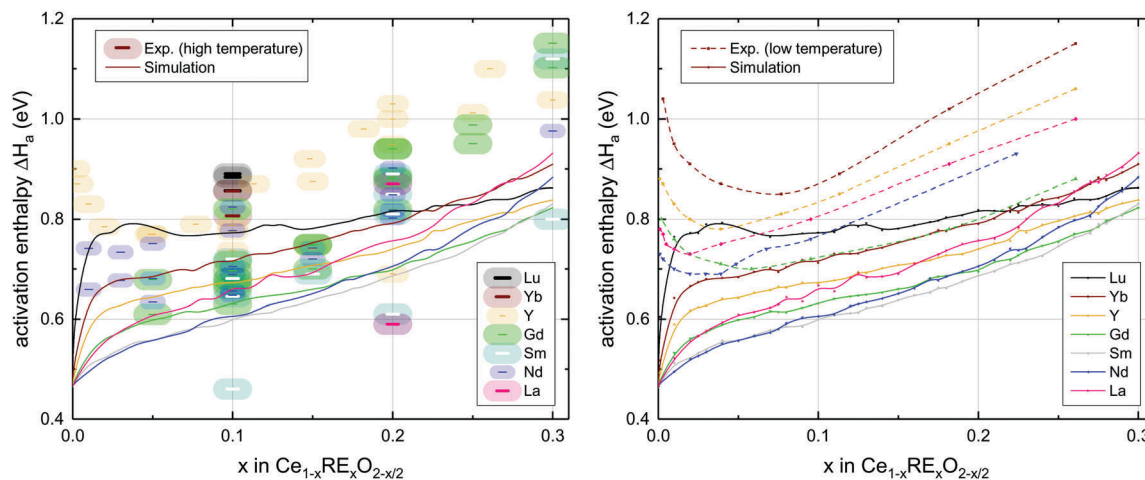


Fig. 25 Activation enthalpy from KMC simulation in this work (lines) and experiments between room temperature and 330 °C (dashed lines)⁸⁶ or higher temperatures up to 1000 °C (dashes) for Lu,^{82,83} Yb,⁸³ Er,⁸³ Y,^{83–85,87,88,98} Dy,^{67,83} Gd,^{61,83,85,87,88,91,92,94} Eu,⁹⁶ Sm,^{72,83,88,98,107} Nd^{74,83,88,100,101} and La doped ceria.⁸⁷

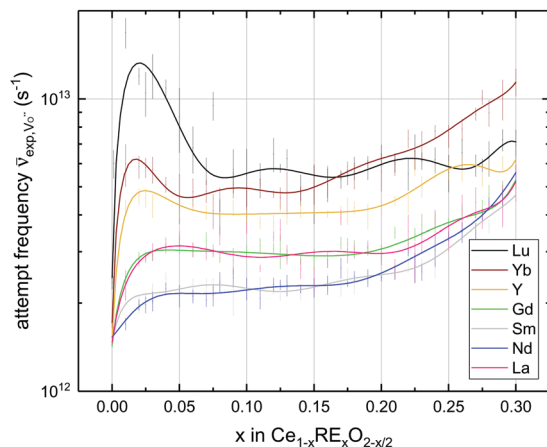


Fig. 26 Apparent attempt frequency for the simulated conductivity of rare-earth doped ceria at 500 °C. Lines are a guide to the eye only.

concentration correlates in conductivity and activation enthalpy, *e.g.* high conductivities are found for low activation enthalpies. Both effects were already found in experiments (see Section 2.3) and are expected since the activation enthalpy dominates the conductivity according to eqn (8) and (9). The ranking order between different dopants is similar in simulations and experiments; even the crossing between the activation enthalpies of La and Gd doped ceria at low dopant fractions is found in simulations similar to the work of Faber *et al.* (dashed lines in Fig. 25).⁸⁶ Exceptions are low activation enthalpies in simulations for Nd doped ceria at all dopant fractions and high activation enthalpies in simulations for La doped ceria at high dopant fractions. However, for the former, the experimental ionic conductivity strongly scatters between different groups and, for the latter, only a few activation enthalpies are reported.

Similar to the conductivity, the activation enthalpy can be calculated for KMC simulations with all or only selected interactions.¹⁶⁹ Either trapping or blocking was neglected. Both influence the final activation enthalpy. Again, the no-trapping case and the only different Ce-RE edges case are similar. Here, the activation enthalpy increases with increasing Ce-RE edge energy and increasing dopant fraction. Again, the no-blocking and the only different $1_{NN} \leftrightarrow 2_{NN}$ RE-V jump case differ. Here, the activation enthalpy increases with increasing $|2_{NN}-1_{NN}|$ and $3_{NN}-2_{NN}$ RE-V association energy differences and increasing dopant fraction. Again, the increase occurs especially at large dopant fractions if the $|2_{NN}-1_{NN}|$ RE-V association energy difference is small (*e.g.* for Nd doped ceria). We conclude that, similar to the maximum ionic conductivity, the activation enthalpy is dominated by trapping.

Macroscopic activation enthalpies for the KMC simulations can also be calculated for lower temperatures, *e.g.* between 267 °C and 500 °C. A shift to mostly higher activation enthalpies can be found. This is expected since less thermal energy is available for successful jumps with high migration barriers. Here, the high migration energies strongly influence the activation enthalpy. This has already been shown in an earlier publication¹⁰⁸ using a simple migration energy model.

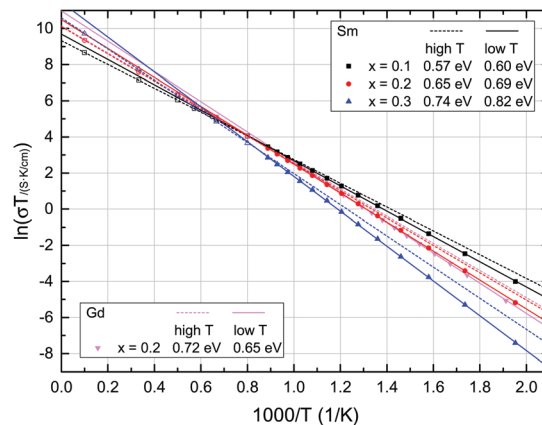


Fig. 27 Ionic conductivity of $Ce_{1-x}RE_xO_{2-x/2}$ as a function of temperature. KMC simulations were performed for Sm and Gd doped ceria. A low and a high temperature region can be found with different activation enthalpies.

The difference in activation enthalpy for the low temperature region (between 267 °C and 500 °C) and the high temperature region (between 500 °C and 600 °C) can be used to calculate an ‘apparent association energy’ as proposed in experiments (see Section 2.3), especially similar to Omar *et al.*⁸³ The resulting apparent association energies are small (<0.03 eV). This is in agreement with the discussed experimental literature, which reports no distinct kink or no kink in the Arrhenius behavior of the conductivity.⁸³ Distinct kinks as reported in experiments by Zhan *et al.*⁷² and Zhang *et al.*⁸⁵ (Fig. 5) can be found in KMC simulations for higher temperatures as shown in Fig. 27 with apparent association energies up to 0.08 eV. In summary, our simulations confirm that the apparent activation enthalpy is influenced by the RE-V association energy. However, the RE-V association energy cannot be extrapolated from experiment, for example due to its dependence on the dopant fraction, as already discussed in Section 2.

5 Conclusions

In this work, the ionic conductivity in the bulk of doped ceria was investigated using theoretical calculations, namely density functional theory (DFT) calculations and Kinetic Monte Carlo (KMC) simulations, and experiments. For a detailed understanding of the underlying mechanism that determines the magnitude of the oxygen ion conductivity and the optimal dopant concentration, the influence of microscopic defect interactions on the macroscopic conductivity was shown. Migration barriers were investigated for energy contributions that are symmetric and asymmetric for forward and backward jumps, which are referred to as blocking and trapping. We defined a general model for the migration energy with a variable number of parameters and chose a model which fits well with the DFT migration energies and uses only a small number of parameters. Subsequently, we used the migration energies of only a few jump configurations to predict the parameters of our model. Our main conclusions are

- The ionic conductivity is influenced by trapping, blocking and vacancy–vacancy interactions.
- Blocking mainly limits the dopant fraction at the ionic conductivity maximum. Here, the migration edge with one dopant is decisive. This blocking effect is strongly underrated in the literature.
- Trapping mainly limits the maximum ionic conductivity value. Here, the association energy differences are decisive.
- Similar to the maximum ionic conductivity, the apparent activation enthalpy is predominantly influenced by trapping.
- No minimum in the apparent activation enthalpy is necessary to reproduce the maximum in the ionic conductivity as a function of dopant fraction.
- The highest conductivity can be found if all absolute values of the association energy differences are small. The $2_{\text{NN}} \leftrightarrow 1_{\text{NN}}$ RE–V association leads to the formation of associates, *i.e.* vacancies are *held* by the dopants as their movement is hindered. The long-range $3_{\text{NN}} \leftrightarrow 2_{\text{NN}}$ RE–V association *catches* vacancies into the vicinity of dopants. Both catch-and-hold need to be small for a large ionic conductivity. The catch-and-hold principle easily predicts the dopant that leads to the highest ionic conductivity.

In this work, we predicted the ionic conductivity of rare-earth doped ceria better than previous KMC simulations using energies from DFT calculations. For comparison, impedance measurements of Sm doped ceria were performed. The experiments agree well with the data predicted by theoretical methods.

Ionic conductivity maxima can be found in a variety of materials including fluorite-structured, perovskite-structured and apatite-type oxides. We believe that trapping, blocking and vacancy–vacancy interactions influence the ionic conductivity in many of these materials. Blocking effects, for example, are caused by doping at the migration edge in fluorite-structured oxides like ceria, while in perovskite-structured oxides like LaGaO₃ or Ba_{0.5}Sr_{0.5}Co_{0.8}Fe_{0.2}O_{3–δ} a migration triangle^{136,172,173} can be found. Therefore, the detailed results and insights obtained here for doped ceria can be generalized and applied to other ion conductors that are important for SOFCs and SOECs, resistive switching materials²²⁴ as well as solid state batteries.

Ionic conductivity maxima can be found in a variety of materials including fluorite-structured, perovskite-structured and apatite-type oxides. We believe that trapping, blocking and vacancy–vacancy interactions influence the ionic conductivity in many of these materials. Blocking effects, for example, are caused by doping at the migration edge in fluorite-structured oxides like ceria, while in perovskite-structured oxides like LaGaO₃ or Ba_{0.5}Sr_{0.5}Co_{0.8}Fe_{0.2}O_{3–δ} a migration triangle^{136,172,173} can be found. Therefore, the detailed results and insights obtained here for doped ceria can be generalized and applied to other ion conductors that are important for SOFCs and SOECs, resistive switching materials²²⁴ as well as solid state batteries.

Conflicts of interest

There are no conflicts to declare.

Appendix

Theoretical details

The ionic conductivity σ_i of the oxygen ions ($i = \text{O}^{2-}$) or vacancies ($i = \text{V}_{\text{O}}^{\bullet\bullet}$) is proportional to their squared charge $z_i^2 e^2$, concentration n_i and mechanical mobility b_i (eqn (8)). For non-interacting defects, the mobility is related to the diffusion coefficient D_i by the classical Einstein relation with the Boltzmann constant k_{B} and the absolute temperature T . Though this approximation fails for most doped materials, it is often used to analyze experimental results. Both diffusion coefficients ($D_{\text{O}^{2-}}$ and $D_{\text{V}_{\text{O}}^{\bullet\bullet}}$) depend on the weighted mean jump rate

of all oxygen ions ($\bar{\Gamma}_{\text{O}^{2-}}$) or vacancies ($\bar{\Gamma}_{\text{V}_{\text{O}}^{\bullet\bullet}}$) to one nearest neighbor site. In this work, jumps to other lattice sites are neglected according to Nakayama and Martin.⁴⁴ In eqn (8), l is the jump distance and γ is the geometrical factor, which includes the number of jump sites n_{p} and the dimension of diffusion d and is $\gamma = \frac{n_{\text{p}}}{2d} = 1$ in a primitive cubic lattice, *e.g.* the oxygen sublattice in ceria.^{174,175} The jump rate can be described by an Arrhenius equation (eqn (9)) with the apparent activation enthalpy ΔH_{a} . The apparent activation enthalpy describes the experimentally determined dependence of the diffusion coefficient on temperature and can be calculated from the slope of the plot $\ln \bar{\Gamma}_i$ versus $1/T$.

$$\sigma_i = n_i \cdot z_i^2 e^2 \cdot b_i, \text{ where } b_i = \frac{D_i}{k_{\text{B}} T} \text{ and } D_i = \gamma l^2 \cdot \bar{\Gamma}_i. \quad (8)$$

$$\bar{\Gamma}_i = \bar{\nu}_{\text{exp},i} \cdot e^{-\frac{\Delta H_{\text{a}}}{k_{\text{B}} T}} \quad (9)$$

Therefore, the pre-exponential factor for diffusion $D_{0,i} = \gamma l^2 \cdot \bar{\nu}_{\text{exp},i}$ depends on the mean experimental attempt frequency $\bar{\nu}_{\text{exp},i}$, which was already discussed in detail in our earlier publication.¹⁰⁸ Naturally, deviations in the activation enthalpy, which appears in the exponential term, possess a stronger influence on the jump rate than deviations in the attempt frequency.

As a result, the activation enthalpy can be extracted from the conductivity according to

$$\sigma_i = \frac{A}{T} e^{-\frac{\Delta H_{\text{a}}}{k_{\text{B}} T}} \quad (10)$$

with the parameter A . In doped ceria, a variety of ionic configurations occur, which lead to a variety of jump environments and possibly different local attempt frequencies. The extracted activation enthalpy ΔH_{a} is therefore a macroscopic property influenced by all jumps.

Computational details

Quantum mechanical calculations were performed using the Vienna *Ab initio* Simulation Package (VASP)^{176,177} calculating geometric parameters and energies at zero temperature. All *ab initio* calculations were carried out within the scope of the density functional theory (DFT) using the Generalized Gradient Approximation (GGA) according to Perdew, Burke and Ernzerhof (PBE)¹⁷⁸ and the projector augmented-wave method (PAW).¹⁷⁹ Alternative methods like Local Density Approximation (LDA) and hybrid functionals (*e.g.* Heyd–Scuseria–Ernzerhof, HSE) have been investigated in the literature.¹⁸⁰ Hafner discusses the advantages of the different exchange–correlation-functionals.¹⁸¹

For plane waves, an energy cut-off of 500 eV was chosen. Supercells consisting of between 8 unit cells (a multiplication of $2 \times 2 \times 2$ unit cells in each dimension) and 64 unit cells ($4 \times 4 \times 4$) were employed. Monkhorst–Pack k -point meshes between $2 \times 2 \times 2$ for the $2 \times 2 \times 2$ supercell and $1 \times 1 \times 1$ for the $3 \times 3 \times 3$ supercell or larger supercells were investigated.

The $5s^2 5p^6 6s^2 5d^1 4f^1$ electrons of the cerium atoms were treated as valence electrons. Similarly, the $5s^2 5p^6 6s^2 5d^1$ electrons of the

lanthanum, neodymium and samarium atoms, the $5p^6 6s^2 5d^1$ electrons of the gadolinium, erbium, thulium and lutetium atoms, the $5p^6 6s^2$ electrons of the ytterbium atoms, the $3s^2 3p^6 3d^1 4s^2$ electrons of the scandium atoms, the $4s^2 4p^6 4d^1 5s^2$ electrons of the yttrium atoms, the $3p^6 3d^5 4s^2$ electrons of the manganese atoms and the $2s^2 2p^4$ electrons of the oxygen atoms were treated as valence electrons.

To account for the localization of strongly correlated f -electrons, a Hubbard U parameter was introduced by the rotational invariant approach.¹⁸² A repulsion parameter of $U = 5$ eV for the $4f$ -orbitals of cerium was chosen according to earlier studies^{42,130,145,147,148,183–186} though other values have also been proposed.^{180,187–192}

The total number of electrons in the cell was adapted for all defective cells to reproduce the actual charge state of the defects according to eqn (1), e.g. $(\text{Ce}_{108}\text{O}_{215})^{2+}$ for a $3 \times 3 \times 3$ supercell containing one oxygen vacancy. Though charge-neutral cells containing defects according to eqn (1) without adjustment of the number of electrons would be preferable, in this work interactions between defects shall be limited. Therefore, charge-neutral cells with large distances between defects are virtually divided into oppositely charged cells. Charged cells are calculated by VASP assuming a neutralizing background charge, which is a valid approach as shown in the literature.^{193–196}

The convergence parameters for electronic and ionic relaxation were set to at least 10^{-5} eV and 10^{-2} eV \AA^{-1} , respectively, to guarantee a sufficient accuracy of the calculated forces.

A lattice constant of 5.49 \AA was calculated for defect-free ceria using the Birch–Murnaghan equation of state, which is larger than the experimental lattice parameter due to the chosen set of parameters,^{197–199} and applied for all calculations as performed in the literature.^{53,54,200} For all calculations, the internal atomic positions in the cell were relaxed (changed to minimize the energy of the cell) without changing the lattice parameter.

The interaction energy (association or repulsion energy) is the energy which is required to move two defects from an infinite distance towards adjacent lattice sites. Possible defects are oxygen vacancies ($\text{V}_\text{O}^\bullet$ abbreviated as V) and dopant cations (RE'_{Ce} abbreviated as RE). Possible distances between defects are numbered consecutively with 1_{NN} being the nearest neighbor position and 2_{NN} the next nearest neighbor position. As an infinitely large defect distance in an infinitely large supercell cannot be calculated, interaction energies are approximated as the difference to the largest calculated defect distance. The right choice of the largest calculated defect distance, which is in the following referred to as termination, is discussed in this work. In an earlier publication,⁴⁶ interaction energies including up to 2_{NN} RE–V and 3_{NN} V–V (cut-off radius 4.7 \AA)⁴⁶ were used, while in this work 2_{NN} RE–V and 4_{NN} V–V (cut-off radius 5.5 \AA) are used as discussed in Section 3.1.

The nudged elastic band method (NEB)^{201–203} was applied to investigate the transition states and the minimum energy

pathways. The ionic configuration for the saddle point configuration ('image') was interpolated from the initial and final state of the migration process. During the NEB calculations, the atom positions of the interpolated image are relaxed whereat an artificially introduced spring force (-5 eV \AA^{-1}) counteracts the deviation of atom positions compared to adjacent images (here: initial and final state).

Tests with more than one intermediate image between the initial and final configuration of the migration showed no differences in the migration energies. The same is true for tests using the climbing image nudged elastic band method (CI-NEB).²⁰⁴ For the latter, deviations in the lattice geometry of only ± 0.0001 \AA were found. Selected jump configurations were also successfully compared with the improved dimer method.^{205,206} Only doping with several Sc dopants causes severe problems during the NEB calculation due to the small ionic radius of Sc, which leads to large lattice distortions leading to very low solubility of Sc in ceria.

Association and migration energies strongly depend on the finite supercell size due to the interactions of the defects with their image in other cells. Therefore, in the literature, generally large supercell sizes are recommended. Alternatively, Freysoldt *et al.* propose a method based on the local electrostatic potential given by VASP to correct electrostatic finite size errors. In this work, the Freysoldt method did not lead to the desired result due to the extended defect clusters.²⁰⁷

Makov and Payne formulated an analytic expression to correct the electrostatic energy created by periodic boundary conditions in calculations.²⁰⁸ The energy of an isolated defect E_{isolated} is given by the calculated energy E_{finite} by

$$E_{\text{isolated}} = E_{\text{finite}} + \frac{\alpha \cdot q^2}{2\epsilon L} + \frac{2\pi \cdot qQ}{3\epsilon L^3} + O(L^{-5}) \quad (11)$$

with the Madelung constant α depending on the type of lattice structure, the charge q and the quadrupole moment of the defect Q , the linear dimension of the supercell $L \propto V^{1/3}$ proportional to the third root of the volume of the supercell V , dielectric constant ϵ and unspecified function O depending on L^{-5} , which may be neglected for larger supercell sizes.

As both interaction and migration energies depend only on differences between two cells, the monopole interaction (L^{-1}) is neglected. In this work, the dipole interaction (L^{-3}) is corrected. Therefore, different supercell sizes are fitted as a function of volume. Eqn (11) is only valid for cubic supercells. Non-cubic supercells, which were still used in an earlier work from the year 2014,⁴⁶ lead to major deviations.

Compared to earlier works from 2009⁴⁴ and 2014,⁴⁶ three major changes to the calculation of the interaction energy were made: termination and finite size correction.

Firstly, the interaction energy strongly depends on the supercell sizes. As a result, the interaction energy was extrapolated to an infinitely large supercell to avoid any size dependencies using finite size correction. While we used a $2 \times 2 \times 2$ supercell in 2009,⁴⁴ we extrapolated to an infinitely large supercell in the work from 2014⁴⁶ and in this work. It should be

|| Actually, cells with isolated defects can be used. However, earlier investigations^{44,46} show that this method may introduce major errors.

noted that the extrapolations in the work from 2014 and this work are different: in this work, the extrapolation was performed using cubic supercells ($2 \times 2 \times 2$ and $3 \times 3 \times 3$), while for the work from 2014 non-cubic supercells were also used, which is not ideal.

Secondly, the interaction energy is defined as the energy that is required to move two defects from an infinite distance towards adjacent lattice sites. On the one hand, infinite distances necessary for the so-called ‘infinite termination’ are difficult to calculate. On the other hand, interaction energies are usually only calculated for a selected defect distance. Any further interactions are assumed to be zero. Therefore, it seems obvious to use the first interaction, which is assumed to be zero (e.g. at 6 Å RE–V distance), directly as a reference for ‘termination at the first neglected interaction’.

To compare both types of termination, it may be assumed that the interaction energy is identical to a fictive Coulomb energy according to eqn (2). Adjacent defects, nearby defects and widely separated defects are distinguished. While an adjacent defect is on a nearest neighbourhood site (1_{NN}) or in close vicinity up to i_{NN} , nearby defects are just outside of the considered interaction radius on $(i + 1)_{\text{NN}}$. Here, for infinite termination, the energy difference between ionic configurations with adjacent defects and widely separated defects is well defined. However, the energy difference of nearby defects compared to adjacent defects just outside of the considered interaction radius is too large. For a termination at the first neglected interaction, the latter is well defined. However, the energy difference of nearby defects compared to widely separated defects is now assumed to be too low. Instead, their energy is equivalent to adjacent defects.

Thus, both types of terminations keep the ranking of different configurations while for the termination at the first neglected interaction also the energies between defects just outside of the considered interaction radius are well defined. The latter is of significant importance for KMC simulations and is therefore used in this work.

Compared to the work from 2014, a nearly constant energy shift of 0.05–0.1 eV to lower absolute energies for this work was found. Main reason for this energy shift is the ‘termination at the first neglected interaction’ of the interaction energies as discussed above, where the first interaction, which is assumed to be zero, is used as a reference. Another reason is the new extrapolation method of the energies for different supercells to an infinitely large supercell to avoid any size dependencies using finite size correction.⁴⁶

Thirdly, in the work from 2009,⁴⁴ we found a smaller 1_{NN} V–V repulsion energy (0.77 eV), not because of the missing finite-size correction as suggested earlier,⁴⁶ but because of the missing Hubbard U parameter and the different termination. A Hubbard U parameter was used in the work from 2014 and this work.

Besides the interaction energies, also the edge energies were calculated differently. While in our earlier publications,^{44,46} edge energies were only calculated in a $2 \times 2 \times 2$ supercell, in this paper edge energies are extrapolated from a $2 \times 2 \times 2$ and a $3 \times 3 \times 3$ supercell to an infinitely large supercell.

Kinetic Monte Carlo

In the literature, the oxygen ion conductivity in ceria was calculated using analytical models^{33,34} and Kinetic Monte Carlo (KMC) simulations.^{38,45,46,132,145,151,153,160,166–168}

The KMC method can be used to simulate kinetic processes in a system dynamically from state to state like the oxygen ion migration.^{38,209} Instead of propagating the classical equations of motions forward in time and simulating atomic vibrations in time steps of about 10^{-15} s, which is done in molecular dynamics (MD),^{210–212} KMC simulations use the knowledge that systems typically evolve with time through diffusive jumps from state to state.²¹³ These occasional jumps shall be limited by an energy barrier $E_{\text{mig},i,j}$, which has to be surmounted by the system for each atom i and each corresponding pathway j .

As the transition rate $\Gamma_{i,j} = \nu_{0,i,j} \cdot e^{-\frac{\Delta E_{\text{mig},i,j}}{k_B T}}$ with the attempt frequency $\nu_{0,i,j}$ depends only on the initial and transition state according to the transition state theory,^{214,215} the KMC method is again a Markov process. In this work, we assume that the attempt frequency $\nu_{0,i,j} = \nu_{0,\text{base}}$ is similar for all jump configurations as test calculations with multiple attempt frequencies showed only a minor influence on the conductivity. We use the attempt frequency in pure ceria at constant volume ($1.47 \times 10^{12} \text{ s}^{-1}$), which was calculated in an earlier work.¹⁰⁸ This value is lower than the ‘typical value’ of 10^{13} s^{-1} , which is applied in many KMC studies. Furthermore, this used value is lower than the value calculated by Dholabhai *et al.* using DFT ($5 \times 10^{12} \text{ s}^{-1}$)¹⁶⁶ and the value calculated by Tarancón *et al.* using classical molecular dynamics, which is $(5.4 \pm 0.3) \times 10^{12} \text{ s}^{-1}$ for the Ce–Ce and Ce–Gd edge in $\text{Ce}_{0.92}\text{Gd}_{0.08}\text{O}_{1.96}$.²¹⁶ The ionic conductivity increases proportionally to the attempt frequency.

Practically, an ideal three-dimensional fluorite-structured lattice consisting of a cation- and anion sublattice is created and filled randomly according to eqn (1) with cerium or dopant ions and oxygen ions or oxygen vacancies, respectively. An oxygen vacancy and jump direction is randomly chosen and the jump is performed, if a random number in the interval $[0,1[$

is smaller than the Boltzmann probability $p_{i,j} = e^{-\frac{\Delta E_{\text{mig},i,j}}{k_B T}}$. The latter is repeated until the number of successful jumps reaches a prespecified number of Monte Carlo steps per particle (oxygen ion).²¹⁷

The time for each Monte Carlo step Δt is given by the total jump rate $\Gamma_{\text{total}} = \sum_i \sum_j \Gamma_{i,j}$, which is the sum of all rates for each vacancy or atom i and each corresponding pathway j . Analogous to a first-order exponential decay process, the probability that a jump has not been performed is given by $p_{\text{survival}} = e^{-\Gamma_{\text{total}} \Delta t}$ and the elapsed time $\Delta t = -\frac{1}{\Gamma_{\text{total}}} \ln(r)$ can be drawn with a random number r from the interval $]0,1[$.²¹³ For ceria in thermodynamic equilibrium, the average time is

$$\langle \Delta t \rangle = \frac{1}{\langle \Gamma_{\text{total}} \rangle} = \left(\sum_{i=1}^{N_V} \sum_{j=1}^6 \langle \Gamma_{i,j} \rangle \right)^{-1} \quad (12)$$

with the number of oxygen vacancies N_V and

$$\begin{aligned} \langle \Gamma_{ij} \rangle &= \left\langle \nu_{0,\text{base}} \cdot e^{-\frac{\Delta E_{\text{mig},ij}}{k_B T}} \right\rangle \\ &= \nu_{0,\text{base}} \frac{\text{MCS}}{N_{\text{att}}} \end{aligned} \quad (13)$$

with the number of Monte Carlos Steps MCS, the number of jump attempts N_{att} and the attempt frequency for all jumps $\nu_{0,\text{base}}$. This results in the total physical time span per simulation

$$t = \text{MCS} \cdot \langle \Delta t \rangle = \frac{N_{\text{att}}}{6N_V \cdot \nu_{0,\text{base}}} \quad (14)$$

For doped ceria, typically used numbers of Monte Carlos Steps and total physical time spans are 100 times the number of oxygen ions and 10^{-6} s, respectively. At low temperature, jumps are rarely accepted and the number of jump attempts increases rapidly. In the ‘dynamic scaling’ method, jump probabilities are scaled by a factor A such that the most probable transition, which has at least 100 jump attempts cumulated with more probable transitions within 10^9 total jump attempts, has the probability 1. This decreases the computation time by a factor A without any impact on the accuracy of the calculations according to our test simulations. The simulated physical time span has to be multiplied with A in this method.

Commonly, the ionic conductivity is calculated from the mean displacement of oxygen ions. For this purpose, the mean displacement is transformed into a tracer diffusion coefficient that can be converted into mechanical mobility using the classical Einstein relation (eqn (8)) for non-interacting defects. However, in doped ceria, non-dilute concentrations lead to a correlation of motion of the ions and the Einstein relation cannot be applied. Here, a small electric field with the strength ε_x is applied in the x -direction and the oxygen ion conductivity is calculated from the mean displacement of all oxygen ions $\langle x \rangle$ in the field direction:^{45,46,218–220}

$$\sigma = \frac{\langle x \rangle}{\varepsilon_x t} q n_V \quad (15)$$

where q and n_V are the charge and concentration of the oxygen vacancies, respectively. The conductivity is identical for electric field directions along all three basis vectors of the unit cell as all directions are isotropic. Test calculations showed identical conductivities if an electric field in all three directions of the lattice, *i.e.* (111) direction, is used. The electric field strength has to be chosen large enough to induce a significant mean displacement and small enough to ensure a linear relationship between mean displacement and field strength, which was verified in this work.⁴⁵ The mean displacement must be investigated in thermodynamic equilibrium; therefore, the anion sublattice has to be equilibrated by a previous KMC simulation.

KMC simulations were performed using the in-house developed software iCon¹⁷⁰ according to an earlier work in a $16 \times 16 \times 16$ supercell with 49 152 ions or vacancies and periodic boundary conditions.⁴⁶

Random lattice configurations were used. Anion sublattices were at first equilibrated by 100 Monte Carlo steps per particle. For low temperatures, lattices were equilibrated at higher temperature, and subsequently only 10 Monte Carlo steps per particle for equilibration were used.

An electric field strength of $0.1 \frac{k_B T}{ql}$ with the charge of the oxygen ion q and the jump distance l was used, which had no influence on the thermodynamic equilibrium according to an earlier work.⁴⁵ Dynamical scaling was activated for temperatures below 500 °C where up to $10^{-5}\%$ of the most probable jumps from a sampling size of 5×10^9 were always accepted. Tests confirm no influence of the dynamical scaling on the ionic conductivity.

Simulations of the ionic conductivity were repeated at least ten times each with 100 Monte Carlo Steps per particle. The standard error on the conductivity results primarily from the use of different starting lattices.

Though we thoroughly discussed the change in the lattice parameter as a function of dopant fraction (Section 2.1), we decided to neglect this influence here due to experimental scattering and use the lattice parameter of pure ceria for all simulations. However, this influence can be easily understood from eqn (8). For an increasing jump distance l , the concentration of the charge carriers decreases with $n_i \propto l^{-3}$ and the diffusion constant increases with $D_i \propto l^2$. As a result, the conductivity is inversely proportional to the lattice parameter. The result is similar for eqn (14) and (15). Here, the electric field strength ε_x is considered for both the jump probabilities, which influences the number of jump attempts N_{att} , and the calculation of the conductivity (eqn (15)). Larger lattice parameters lead to lower fields in the jump probabilities. The underestimated lattice parameter of a finished KMC simulation can be corrected by decreasing the electric field strength in eqn (15) accordingly. At the same time, the mean displacement of all oxygen ions $\langle x \rangle$ in the field direction has to be increased with the lattice parameter.

Experimental details

Samples were prepared by dissolving cerium(III) nitrate hexahydrate (99.9%, Chempur) and citric acid (VWR International, 2.5 equivalents) in water. During mixing for several hours at 50 °C the sol-gel transformation occurred. The temperature was increased to 350 °C where the produced foam was dried for three hours and subsequently calcined for four hours at 1000 °C. The calcined powder was dry milled in a planetary mill, uniaxially pressed to disks (10 mm in diameter and 2 mm thick) and sintered in air at 1400 °C for 24 hours. The composition was successfully verified using X-ray diffraction (Theta-Theta diffractometer, STOE, Darmstadt, Germany). Density measurements according to the Archimedes method gave high densities around 98% of the theoretical value. For impedance measurements, samples were coated with platinum paste and connected with a platinum wire. Impedance spectroscopy measurements were performed in air using a two-point geometry (Solatron 1260) with frequencies between 10^7 and 7×10^{-2} Hz. The bulk semicircle was identified according to the literature.²²¹ The depressed bulk

semicircle in the complex impedance plot was analyzed using an equivalent circuit composed of an RQ-element with the constant phase element Q. Further details will be presented in an upcoming paper.²²² The ionic conductivity was calculated according to $\sigma = \frac{d}{AR}$ with the sample thickness d and the area A .

Acknowledgements

The authors gratefully acknowledge the computing time granted by the JARA-HPC Vergabegremium and provided on the JARA-HPC Partition part of the supercomputer JURECA at Forschungszentrum Jülich.²²³ Simulations were performed with computing resources granted by RWTH Aachen University under project rwth0010. The authors gratefully acknowledge the computing time granted by the JARA-HPC Vergabegremium and provided on the JARA-HPC Partition part of the supercomputer CLAIX at RWTH Aachen University. We thank the Jülich Supercomputing Centre for granting computing time within the project HDA160. Financial support of the German Federal Ministry of Economics and Technology within the project HORIZONT is acknowledged. Funding from the German Research Foundation (DFG) within the collaborative research center, SFB 917 “Nanoswitches”, is gratefully acknowledged. This work is partly supported by the “Materials research by Information Integration” Initiative (MI²I) project of the Support Program for Starting Up Innovation Hub from Japan Science and Technology Agency (JST). Discussions with Roger A. De Souza are gratefully acknowledged.

References

- M. Mogensen, *Solid State Ionics*, 2000, **129**, 63–94.
- N. Q. Minh, *J. Am. Ceram. Soc.*, 1993, **76**, 563–588.
- O. Yamamoto, *Electrochim. Acta*, 2000, **45**, 2423–2435.
- M. F. Trubelja and V. S. Stubican, *J. Am. Ceram. Soc.*, 1991, **74**, 2489–2494.
- T. Ishihara, H. Matsuda and Y. Takita, *J. Am. Chem. Soc.*, 1994, **116**, 3801–3803.
- P.-N. Huang, *J. Electrochem. Soc.*, 1996, **143**, 1644.
- A. Petric, *Solid State Ionics*, 1996, **92**, 113–117.
- T. L. Nguyen, M. Dokiya, S. Wang, H. Tagawa and T. Hashimoto, *Solid State Ionics*, 2000, **130**, 229–241.
- L. Dunyushkina, A. K. Demin and B. V. Zhuravlev, *Solid State Ionics*, 1999, **116**, 85–88.
- S. Beaudet-Savignat, A. Vincent, S. Lambert and F. Gervais, *J. Mater. Chem.*, 2007, **17**, 2078.
- T. Takahashi and H. Iwahara, *Mater. Res. Bull.*, 1978, **13**, 1447–1453.
- T. Takahashi, H. Iwahara and T. Arao, *J. Appl. Electrochem.*, 1975, **5**, 187–195.
- N. M. Sammes, G. A. Tompsett, H. Näge and F. Aldinger, *J. Eur. Ceram. Soc.*, 1999, **19**, 1801–1826.
- P. Haworth, S. Smart, J. Glasscock and J. C. Diniz da Costa, *Sep. Purif. Technol.*, 2011, **81**, 88–93.
- O. Kosasang, K. Somroop, P. Chindaudom and R. Pornprasertsuk, 215th ECS Meeting, 2009, pp. 145–151.
- D. Han, N. Hatada, T. Uda and R. Koc, *J. Am. Ceram. Soc.*, 2016, **99**, 3745–3753.
- D. Han, N. Hatada and T. Uda, *J. Electrochem. Soc.*, 2016, **163**, F470–F476.
- I. M. Markus, N. Adelstein, M. Asta and L. C. de Jonghe, *J. Phys. Chem. C*, 2014, **118**, 5073–5080.
- H. Aono, E. Sugimoto, Y. Sadaoka, N. Imanaka and G.-Y. Adachi, *Chem. Lett.*, 1990, 1825–1828.
- H. Morimoto, M. Hirukawa, A. Matsumoto, T. Kurahayashi, N. Ito and S.-I. Tobishima, *Electrochemistry*, 2014, **82**, 870–874.
- A. Rossbach, F. Tietz and S. Grieshammer, in preparation.
- J. C. Bachman, S. Muy, A. Grimaud, H.-H. Chang, N. Pour, S. F. Lux, O. Paschos, F. Maglia, S. Lupart, P. Lamp, L. Giordano and Y. Shao-Horn, *Chem. Rev.*, 2016, **116**, 140–162.
- J. Christensen, P. Albertus, R. S. Sanchez-Carrera, T. Lohmann, B. Kozinsky, R. Liedtke, J. Ahmed and A. Kojic, *J. Electrochem. Soc.*, 2012, **159**, R1–R30.
- M. Panhans and R. Blumenthal, *Solid State Ionics*, 1993, **60**, 279–298.
- K. Eguchi, T. Setoguchi, T. Inoue and H. Arai, *Solid State Ionics*, 1992, **52**, 165–172.
- R. D. Shannon, *Acta Crystallogr., Sect. A: Cryst. Phys., Diffraction, Theor. Gen. Crystallogr.*, 1976, **32**, 751–767.
- H. Yahiro, *Solid State Ionics*, 1989, **36**, 71–75.
- M. Mogensen, T. Lindegaard, U. R. Hansen and G. Mogensen, *Proceedings of the Second International Symposium on Ionic and Mixed Conducting Ceramics*, Pennington, NJ, 1994, pp. 448–465.
- H. Inaba and H. Tagawa, *Solid State Ionics*, 1996, **83**, 1–16.
- R. Gerhardt-Anderson and A. A. Nowick, *Solid State Ionics*, 1981, **5**, 547–550.
- D. W. Strickler and W. G. Carlson, *J. Am. Ceram. Soc.*, 1965, **48**, 286–289.
- H. Schmalzried, *Z. Phys. Chem.*, 1977, **105**, 47–62.
- D. K. Hohnke, *Solid State Ionics*, 1981, **5**, 531–534.
- M. Martin, *J. Electroceram.*, 2006, **17**, 765–773.
- C. R. Catlow and S. C. Parker, in *Computer Simulation of Solids*, ed. C. Catlow and W. Mackrodt, Springer, Berlin Heidelberg, 1982, vol. 166, pp. 222–242.
- V. Butler, C. Catlow, B. Fender and J. Harding, *Solid State Ionics*, 1983, **8**, 109–113.
- C. Catlow, *Solid State Ionics*, 1984, **12**, 67–73.
- A. Murray, G. Murch and C. Catlow, *Solid State Ionics*, 1986, **18–19**, 196–202.
- N. V. Skorodumova, M. Baudin and K. Hermansson, *Phys. Rev. B: Condens. Matter Mater. Phys.*, 2004, **69**, 075401.
- Z. Yang, T. K. Woo, M. Baudin and K. Hermansson, *J. Chem. Phys.*, 2004, **120**, 7741.
- D. A. Andersson, S. I. Simak, N. V. Skorodumova, I. A. Abrikosov and B. Johansson, *Proc. Natl. Acad. Sci. U. S. A.*, 2006, **103**, 3518–3521.
- A. Ismail, J. Hooper, J. B. Giorgi and T. K. Woo, *Phys. Chem. Chem. Phys.*, 2011, **13**, 6116.
- A. Chronos, B. Yildiz, A. Tarancón, D. Parfitt and J. A. Kilner, *Energy Environ. Sci.*, 2011, **4**, 2774.

- 44 M. Nakayama and M. Martin, *Phys. Chem. Chem. Phys.*, 2009, **11**, 3241–3249.
- 45 B. O. H. Grope, T. Zacherle, M. Nakayama and M. Martin, *Solid State Ionics*, 2012, **225**, 476–483.
- 46 S. Grieshammer, B. O. H. Grope, J. Koettgen and M. Martin, *Phys. Chem. Chem. Phys.*, 2014, **16**, 9974.
- 47 J. Koettgen, P. C. Schmidt, T. Bučko and M. Martin, *Phys. Rev. B*, 2018, **97**, 024305.
- 48 H. Tuller and A. Nowick, *J. Phys. Chem. Solids*, 1977, **38**, 859–867.
- 49 R. Farra, M. García-Melchor, M. Eichelbaum, M. Hashagen, W. Frandsen, J. Allan, F. Girgsdies, L. Szentmiklósi, N. López and D. Teschner, *ACS Catal.*, 2013, **3**, 2256–2268.
- 50 M. V. Ganduglia-Pirovano, J. L. F. Da Silva and J. Sauer, *Phys. Rev. Lett.*, 2009, **102**, 026101.
- 51 T. Holme and F. B. Prinz, *Trans. Mater. Res. Soc. Jpn.*, 2010, **35**, 59–68.
- 52 M. Nakayama, H. Ohshima, M. Nogami and M. Martin, *Phys. Chem. Chem. Phys.*, 2012, **14**, 6079.
- 53 P. R. L. Keating, D. O. Scanlon, B. J. Morgan, N. M. Galea and G. W. Watson, *J. Phys. Chem. C*, 2012, **116**, 2443–2452.
- 54 T. Zacherle, A. Schriever, R. A. De Souza and M. Martin, *Phys. Rev. B: Condens. Matter Mater. Phys.*, 2013, **87**, 134104.
- 55 S. Grieshammer, T. Zacherle and M. Martin, *Phys. Chem. Chem. Phys.*, 2013, **15**, 15935–15942.
- 56 J. J. Plata, A. M. Márquez and J. F. Sanz, *J. Phys. Chem. C*, 2013, **117**, 25497–25503.
- 57 T. H. Etsell and S. N. Flengas, *Chem. Rev.*, 1970, **70**, 339–376.
- 58 D. J. Bevan and E. Summerville, in *Handbook on the Physics and Chemistry of Rare Earths: Non-metallic compounds*, ed. K. A. Gschneidner and L. R. Eyring, North-Holland Pub. Co, 1979, pp. 401–524.
- 59 G. Balazs, *Solid State Ionics*, 1995, **76**, 155–162.
- 60 S. Dikmen, P. Shuk and M. Greenblatt, *Solid State Ionics*, 1999, **126**, 89–95.
- 61 Z. Tianshu, P. Hing, H. Huang and J. Kilner, *Solid State Ionics*, 2002, **148**, 567–573.
- 62 G. Brauer and H. Gradinger, *Die Naturwissenschaften*, 1951, **38**, 559–560.
- 63 W. Mišta, M. A. Małecka and L. Kepiński, *Appl. Catal.*, A, 2009, **368**, 71–78.
- 64 V. Grover, A. Banerji, P. Sengupta and A. Tyagi, *J. Solid State Chem.*, 2008, **181**, 1930–1935.
- 65 M. A. Małecka, L. Kepiński and M. Maczka, *J. Solid State Chem.*, 2008, **181**, 2306–2312.
- 66 B. Matović, M. Stojmenović, J. Pantić, A. Varela, M. Žunić, N. Jiraborvornpongsa and T. Yano, *Journal of Asian Ceramic Societies*, 2014, **2**, 117–122.
- 67 C. Sánchez-Bautista, A. J. Dos santos Garcia, J. Peña-Martínez and J. Canales-Vázquez, *Solid State Ionics*, 2010, **181**, 1665–1673.
- 68 S. A. Acharya, *J. Power Sources*, 2012, **198**, 105–111.
- 69 L. Li, G. Li, Y. Che and W. Su, *Chem. Mater.*, 2000, **12**, 2567–2574.
- 70 P. Shuk, M. Greenblatt and M. Croft, *Chem. Mater.*, 1999, **11**, 473–479.
- 71 S. Zha, C. Xia and G. Meng, *J. Power Sources*, 2003, **115**, 44–48.
- 72 Z. Zhan, T.-L. Wen, H. Tu and Z.-Y. Lu, *J. Electrochem. Soc.*, 2001, **148**, A427.
- 73 L. Aneflous, J. A. Musso, S. Villain, J.-R. Gavarri and H. Benyaich, *J. Solid State Chem.*, 2004, **177**, 856–865.
- 74 L. P. Li, X. M. Lin, G. S. Li and H. Inomata, *J. Mater. Res.*, 2001, **16**, 3207.
- 75 Y. Zheng, Y. Shi, H. Gu, L. Gao, H. Chen and L. Guo, *Mater. Res. Bull.*, 2009, **44**, 1717–1721.
- 76 R. T. Dirstine, *J. Electrochem. Soc.*, 1979, **126**, 264.
- 77 G. Brauer and H. Gradinger, *Z. Anorg. Allg. Chem.*, 1954, **276**, 209–226.
- 78 A. Nakamura, *Solid State Ionics*, 2010, **181**, 1631–1653.
- 79 R. A. De Souza, *Phys. Chem. Chem. Phys.*, 2009, **11**, 9939–9969.
- 80 B. Steele, *Solid State Ionics*, 2000, **129**, 95–110.
- 81 A. Jain, G. Hautier, S. P. Ong and K. Persson, *J. Mater. Res.*, 2016, **31**, 977–994.
- 82 S. Omar, E. Wachsman and J. Nino, *Solid State Ionics*, 2006, **177**, 3199–3203.
- 83 S. Omar, E. D. Wachsman, J. L. Jones and J. C. Nino, *J. Am. Ceram. Soc.*, 2009, **92**, 2674–2681.
- 84 D. Wang, D. Park, J. Griffith and A. Nowick, *Solid State Ionics*, 1981, **2**, 95–105.
- 85 T. Zhang, J. Ma, L. Kong, S. Chan and J. Kilner, *Solid State Ionics*, 2004, **170**, 209–217.
- 86 J. Faber, C. Geoffroy, A. Roux, A. Sylvestre and P. Abélard, *Appl. Phys. A: Solids Surf.*, 1989, **49**, 225–232.
- 87 D. Pérez-Coll, D. Marrero-López, P. Núñez, S. Piñol and J. R. Frade, *Electrochim. Acta*, 2006, **51**, 6463–6469.
- 88 W. Zajac, *Solid State Ionics*, 2008, **179**, 154–158.
- 89 J. van Herle, D. Seneviratne and A. McEvoy, *J. Eur. Ceram. Soc.*, 1999, **19**, 837–841.
- 90 J. Van herle, T. Horita, T. Kawada, N. Sakai, H. Yokokawa and M. Dokiya, *Solid State Ionics*, 1996, **86–88**, 1255–1258.
- 91 B. Steele, K. Zheng, R. Rudkin, N. Kiratzis and M. Cristie, in *Proceedings of the Fourth International Symposium on Solid Oxide Fuel Cells (SOFC-IV)*, ed. M. Dokiya, Electrochemical Society, Pennington, NJ, 1995, vol. 95-1, pp. 1028–1038.
- 92 K. Huang, M. Feng and J. B. Goodenough, *J. Am. Ceram. Soc.*, 1998, **81**, 357–362.
- 93 E. Ruiz-Trejo, J. D. Sirman, Y. M. Baikov and J. A. Kilner, *Solid State Ionics*, 1998, **113–115**, 565–569.
- 94 G. Christie, *Solid State Ionics*, 1996, **83**, 17–27.
- 95 K. R. Reddy and K. Karan, *J. Electroceram.*, 2005, **15**, 45–56.
- 96 N. Cioatera, V. Pârvulescu, A. Rolle and R. N. Vannier, *Solid State Ionics*, 2009, **180**, 681–687.
- 97 R. Sanghavi, R. Devanathan, M. I. Nandasiri, S. Kuchibhatla, L. Kovarik, S. Thevuthasan and S. Prasad, *Solid State Ionics*, 2011, **204–205**, 13–19.
- 98 M. G. Bellino, D. G. Lamas and N. E. Walsöe de Reca, *Adv. Funct. Mater.*, 2006, **16**, 107–113.
- 99 Y. Zheng, M. Zhou, L. Ge, S. Li, H. Chen and L. Guo, *J. Alloys Compd.*, 2011, **509**, 1244–1248.
- 100 I. Stephens and J. Kilner, *Solid State Ionics*, 2006, **177**, 669–676.

- 101 J. X. Zhu, D. F. Zhou, S. R. Guo, J. F. Ye, X. F. Hao, X. Q. Cao and J. Meng, *J. Power Sources*, 2007, **174**, 114–123.
- 102 A. Nowick, D. Wang, D. Park and J. Griffith, in *Fast ion transport in solids*, ed. P. Vashishta, J. N. Mundy and G. K. Shenoy, North Holland, New York, 1979, p. 673.
- 103 C. Tian and S.-W. Chan, *MRS Proc.*, 1998, **548**, 623–629.
- 104 C. Tian, *Solid State Ionics*, 2000, **134**, 89–102.
- 105 M. Mogensen, T. Lindegaard, U. R. Hansen and G. Mogensen, *J. Electrochem. Soc.*, 1994, **141**, 2122.
- 106 R. O. Fuentes and R. T. Baker, *J. Power Sources*, 2009, **186**, 268–277.
- 107 D. Pérez-Coll, P. Núñez and J. R. Frade, *J. Electrochem. Soc.*, 2006, **153**, A478.
- 108 J. Koettgen, T. Zacherle, S. Grieshammer and M. Martin, *Phys. Chem. Chem. Phys.*, 2017, **19**, 9957–9973.
- 109 A. Hammou and J. Guindet, in *The CRC handbook of solid state electrochemistry*, ed. P. J. Gellings and H. J. M. Bouwmeester, CRC Press, Boca Raton and Fla, 1997, pp. 407–444.
- 110 R. N. Blumenthal, P. W. Lee and R. J. Panlener, *J. Electrochem. Soc.*, 1971, **118**, 123.
- 111 H. Arai, *Solid State Ionics*, 1986, **20**, 241–248.
- 112 K. Eguchi, T. Kunishaki and H. Arai, *J. Am. Ceram. Soc.*, 1986, **69**, C-282–C-285.
- 113 H. Yahiro, *Solid State Ionics*, 1986, **21**, 37–47.
- 114 J. M. Ralph, PhD thesis, Imperial College London, 1998.
- 115 D. Steele and B. E. F. Fender, *J. Phys. C: Solid State Phys.*, 1974, **7**, 1–11.
- 116 M. Abraham, R. Weeks, G. Clark and C. Finch, *Phys. Rev.*, 1966, **148**, 350–352.
- 117 T. Ohashi, *Solid State Ionics*, 1998, **113–115**, 559–564.
- 118 S. Yamazaki, *Solid State Ionics*, 2000, **136–137**, 913–920.
- 119 S. Yamazaki, *Solid State Ionics*, 2002, **154–155**, 113–118.
- 120 H. Deguchi, H. Yoshida, T. Inagaki and M. Horiuchi, *Solid State Ionics*, 2005, **176**, 1817–1825.
- 121 P. Jain, H. J. Avila-Paredes, C. Gapuz, S. Sen and S. Kim, *J. Phys. Chem. C*, 2009, **113**, 6553–6560.
- 122 N. Kim and J. F. Stebbins, *Chem. Mater.*, 2007, **19**, 5742–5747.
- 123 H. Maekawa, K. Kawata, Y. P. Xiong, N. Sakai and H. Yokokawa, *Solid State Ionics*, 2009, **180**, 314–319.
- 124 W. O'Neill and M. Morris, *Chem. Phys. Lett.*, 1999, **305**, 389–394.
- 125 T. Y. Tien and E. C. Subbarao, *J. Chem. Phys.*, 1963, **39**, 1041.
- 126 A. Nakamura, *J. Electrochem. Soc.*, 1980, **127**, 2325.
- 127 A. Nakamura, *J. Electrochem. Soc.*, 1986, **133**, 1542.
- 128 D. R. Ou, T. Mori, F. Ye, T. Kobayashi, J. Zou, G. Auchterlonie and J. Drennan, *Appl. Phys. Lett.*, 2006, **89**, 171911.
- 129 D. Ou, T. Mori, F. Ye, J. Zou, G. Auchterlonie and J. Drennan, *Phys. Rev. B: Condens. Matter Mater. Phys.*, 2008, **77**, 024108.
- 130 J. Hooper, A. Ismail, J. B. Giorgi and T. K. Woo, *Phys. Chem. Chem. Phys.*, 2010, **12**, 12969.
- 131 F. Shimojo, T. Okabe, F. Tachibana, M. Kobayashi and H. Okazaki, *J. Phys. Soc. Jpn*, 1992, **61**, 2848–2857.
- 132 M. Meyer and N. Nicoloso, *Ber. Bunsen-Ges.*, 1997, **101**, 1393–1398.
- 133 J. Kilner, *Solid State Ionics*, 1983, **8**, 201–207.
- 134 S. J. Hong and A. V. Virkar, *J. Am. Ceram. Soc.*, 1995, **78**, 433–439.
- 135 D.-J. Kim, *J. Am. Ceram. Soc.*, 1989, **72**, 1415–1421.
- 136 J. Kilner and R. Brook, *Solid State Ionics*, 1982, **6**, 237–252.
- 137 H. Yoshida, *Solid State Ionics*, 2001, **140**, 191–199.
- 138 X. Wei, W. Pan, L. Cheng and B. Li, *Solid State Ionics*, 2009, **180**, 13–17.
- 139 L. Minervini, *Solid State Ionics*, 1999, **116**, 339–349.
- 140 M. Zacate, L. Minervini, D. Bradfield, R. Grimes and K. Sickafus, *Solid State Ionics*, 2000, **128**, 243–254.
- 141 A. Navrotsky, P. Simoncic, H. Yokokawa, W. Chen and T. Lee, *Faraday Discuss.*, 2006, **134**, 171.
- 142 H. Yoshida, *Solid State Ionics*, 2003, **160**, 109–116.
- 143 K. Muthukkumaran, R. Bokalawela, T. Mathews and S. Selladurai, *J. Mater. Sci.*, 2007, **42**, 7461–7466.
- 144 C. Frayret, A. Villesuzanne, M. Pouchard, F. Mauvy, J.-M. Bassat and J.-C. Grenier, *J. Phys. Chem. C*, 2010, **114**, 19062–19076.
- 145 P. P. Dholabhai and J. B. Adams, *J. Mater. Sci.*, 2012, **47**, 7530–7541.
- 146 T. Mori, R. Buchanan, D. Ou, F. Ye, T. Kobayashi, J.-D. Kim, J. Zou and J. Drennan, *J. Solid State Electrochem.*, 2008, **12**, 841–849.
- 147 P. P. Dholabhai, J. B. Adams, P. Crozier and R. Sharma, *Phys. Chem. Chem. Phys.*, 2010, **12**, 7904.
- 148 P. P. Dholabhai, J. B. Adams, P. Crozier and R. Sharma, *J. Chem. Phys.*, 2010, **132**, 094104.
- 149 Z.-P. Li, T. Mori, J. Zou and J. Drennan, *Mater. Res. Bull.*, 2013, **48**, 807–812.
- 150 B. Yildiz, *MRS Bull.*, 2014, **39**, 147–156.
- 151 J. O. Nilsson, M. Leetmaa, O. Y. Vekilova, S. I. Simak and N. V. Skorodumova, *Phys. Chem. Chem. Phys.*, 2017, **19**, 13723–13730.
- 152 A. Ismail, J. B. Giorgi and T. K. Woo, *J. Phys. Chem. C*, 2012, **116**, 704–713.
- 153 A. Oaks, D. Yun, B. Ye, W.-Y. Chen and J. F. Stubbins, *J. Nucl. Mater.*, 2011, **414**, 145–149.
- 154 A. Van der Ven, G. Ceder, M. Asta and P. D. Tepesch, *Phys. Rev. B: Condens. Matter Mater. Phys.*, 2001, **64**, 184307.
- 155 A. Van der Ven and G. Ceder, *Phys. Rev. Lett.*, 2005, **94**, 045901.
- 156 E. Lee, F. Prinz and W. Cai, *Phys. Rev. B: Condens. Matter Mater. Phys.*, 2011, **83**, 052301.
- 157 R. Kikuchi, *Phys. Rev.*, 1951, **81**, 988–1003.
- 158 J. M. Sanchez, F. Ducastelle and D. Gratias, *Phys. A*, 1984, **128**, 334–350.
- 159 R. Krishnamurthy, Y.-G. Yoon, D. J. Srolovitz and R. Car, *J. Am. Ceram. Soc.*, 2004, **87**, 1821–1830.
- 160 S. B. Adler and J. W. Smith, *J. Chem. Soc., Faraday Trans.*, 1993, **89**, 3123.
- 161 S. B. Adler, J. W. Smith and J. A. Reimer, *J. Chem. Phys.*, 1993, **98**, 7613.
- 162 M. Martin, *Z. Phys. Chem.*, 2005, **219**, 105–122.
- 163 R. Pornprasertsuk, P. Ramanarayanan, C. B. Musgrave and F. B. Prinz, *J. Appl. Phys.*, 2005, **98**, 103513.
- 164 F. Shimojo and H. Okazaki, *J. Phys. Soc. Jpn*, 1992, **61**, 4106–4118.
- 165 R. Pornprasertsuk, J. Cheng, H. Huang and F. B. Prinz, *Solid State Ionics*, 2007, **178**, 195–205.

- 166 P. P. Dholabhai, S. Anwar, J. B. Adams, P. Crozier and R. Sharma, *J. Solid State Chem.*, 2011, **184**, 811–817.
- 167 P. P. Dholabhai, J. B. Adams, P. A. Crozier and R. Sharma, *J. Mater. Chem.*, 2011, **21**, 18991.
- 168 P. P. Dholabhai, S. Anwar, J. B. Adams, P. A. Crozier and R. Sharma, *Modell. Simul. Mater. Sci. Eng.*, 2012, **20**, 015004.
- 169 J. Koettgen, PhD thesis, RWTH Aachen University, 2017.
- 170 P. Hein, B. O. H. Grope, J. Koettgen, S. Grieshammer and M. Martin, in preparation.
- 171 J. Koettgen and M. Martin, in preparation.
- 172 R. d. Souza and M. Martin, *Monatsh. Chem.*, 2009, **140**, 1011–1015.
- 173 C. Wessel, M.-W. Lumey and R. Dronskowski, *J. Membr. Sci.*, 2011, **366**, 92–96.
- 174 L. T. Kong and L. J. Lewis, *Phys. Rev. B: Condens. Matter Mater. Phys.*, 2006, **74**, 073412.
- 175 W. D. Kingery, H. K. Bowen and D. R. Uhlmann, *Introduction to ceramics*, Wiley, New York, 2nd edn, 1976.
- 176 G. Kresse and J. Furthmüller, *Phys. Rev. B: Condens. Matter Mater. Phys.*, 1996, **54**, 11169–11186.
- 177 G. Kresse and D. Joubert, *Phys. Rev. B: Condens. Matter Mater. Phys.*, 1999, **59**, 1758–1775.
- 178 J. P. Perdew, K. Burke and M. Ernzerhof, *Phys. Rev. Lett.*, 1997, **78**, 1396.
- 179 P. E. Blöchl, *Phys. Rev. B: Condens. Matter Mater. Phys.*, 1994, **50**, 17953–17979.
- 180 C. Loschen, J. Carrasco, K. Neyman and F. Illas, *Phys. Rev. B: Condens. Matter Mater. Phys.*, 2007, **75**, 035115.
- 181 J. Hafner, *J. Comput. Chem.*, 2008, **29**, 2044–2078.
- 182 S. L. Dudarev, G. A. Botton, S. Y. Savrasov, C. J. Humphreys and A. P. Sutton, *Phys. Rev. B: Condens. Matter Mater. Phys.*, 1998, **57**, 1505–1509.
- 183 M. Nolan, J. E. Fearon and G. W. Watson, *Solid State Ionics*, 2006, **177**, 3069–3074.
- 184 Z. Yang, G. Luo, Z. Lu and K. Hermansson, *J. Chem. Phys.*, 2007, **127**, 074704.
- 185 Z. Yang, G. Luo, Z. Lu, T. K. Woo and K. Hermansson, *J. Phys.: Condens. Matter*, 2008, **20**, 035210.
- 186 M. Nolan, V. S. Verdugo and H. Metiu, *Surf. Sci.*, 2008, **602**, 2734–2742.
- 187 S. Fabris, G. Vicario, G. Balducci, S. D. Gironcoli and S. Baroni, *J. Phys. Chem. B*, 2005, **109**, 22860–22867.
- 188 C. W. M. Castleton, J. Kullgren and K. Hermansson, *J. Chem. Phys.*, 2007, **127**, 244704.
- 189 H. Jiang, R. Gomez-Abal, P. Rinke and M. Scheffler, *Phys. Rev. Lett.*, 2009, **102**, 126403.
- 190 H.-T. Chen, J.-G. Chang, H.-L. Chen and S.-P. Ju, *J. Comput. Chem.*, 2009, **30**, 2433–2442.
- 191 H.-T. Chen and J.-G. Chang, *J. Chem. Phys.*, 2010, **132**, 214702.
- 192 S. Lutfalla, V. Shapovalov and A. T. Bell, *J. Chem. Theory Comput.*, 2011, **7**, 2218–2223.
- 193 T. Zacherle, P. C. Schmidt and M. Martin, *Phys. Rev. B: Condens. Matter Mater. Phys.*, 2013, **87**, 235206.
- 194 J. X. Zheng, G. Ceder, T. Maxisch, W. K. Chim and W. K. Choi, *Phys. Rev. B: Condens. Matter Mater. Phys.*, 2006, **73**, 104101.
- 195 J. Wang, Y. Du, H. Xu, C. Jiang, Y. Kong, L. Sun and Z.-K. Liu, *Phys. Rev. B: Condens. Matter Mater. Phys.*, 2011, **84**, 024107.
- 196 X. Li, M. W. Finnis, J. He, R. K. Behera, S. R. Phillpot, S. B. Sinnott and E. C. Dickey, *Acta Mater.*, 2009, **57**, 5882–5891.
- 197 F. D. Murnaghan, *Am. J. Math.*, 1937, **59**, 235.
- 198 F. D. Murnaghan, *Proc. Natl. Acad. Sci. U. S. A.*, 1944, **30**, 244–247.
- 199 F. Birch, *Phys. Rev.*, 1947, **71**, 809–824.
- 200 J. L. F. Da Silva, M. V. Ganduglia-Pirovano, J. Sauer, V. Bayer and G. Kresse, *Phys. Rev. B: Condens. Matter Mater. Phys.*, 2007, **75**, 045121.
- 201 G. Mills, H. Jónsson and G. K. Schenter, *Surf. Sci.*, 1995, **324**, 305–337.
- 202 H. Jónsson, G. Mills and K. M. Jacobsen, in *Classical and quantum dynamics in condensed phase simulations*, ed. B. J. Berne, World Scientific, Singapore, 1998, pp. 385–404.
- 203 M. Lumeij, J. Koettgen, M. Gilleßen, T. Itoh and R. Dronskowski, *Solid State Ionics*, 2012, **222–223**, 53–58.
- 204 G. Henkelman, B. P. Uberuaga and H. Jónsson, *J. Chem. Phys.*, 2000, **113**, 9901.
- 205 G. Henkelman and H. Jónsson, *J. Chem. Phys.*, 1999, **111**, 7010.
- 206 A. Heyden, A. T. Bell and F. J. Keil, *J. Chem. Phys.*, 2005, **123**, 224101.
- 207 C. Freysoldt, J. Neugebauer and C. van de Walle, *Phys. Rev. Lett.*, 2009, **102**, 016402.
- 208 G. Makov and M. C. Payne, *Phys. Rev. B: Condens. Matter Mater. Phys.*, 1995, **51**, 4014–4022.
- 209 G. E. Murch, *Am. J. Phys.*, 1979, **47**, 78.
- 210 C. W. Huang, W. Wei, C. S. Chen and J. C. Chen, *J. Eur. Ceram. Soc.*, 2011, **31**, 3159–3169.
- 211 J. Klarbring, O. Y. Vekilova, J. O. Nilsson, N. V. Skorodumova and S. I. Simak, *Solid State Ionics*, 2016, **296**, 47–53.
- 212 J. A. Purton, N. L. Allan and D. S. Gunn, *Solid State Ionics*, 2017, **299**, 32–37.
- 213 A. F. Voter, in *Radiation effects in solids*, ed. K. E. Sickafus, E. A. Kotomin and B. P. Uberuaga, Springer, Dordrecht, 2007, vol. 235, pp. 1–23.
- 214 H. Eyring, *J. Chem. Phys.*, 1935, **3**, 107.
- 215 G. H. Vineyard, *J. Phys. Chem. Solids*, 1957, **3**, 121–127.
- 216 A. Tarancón, A. Morata, F. Peiró and G. Dezanneau, *Fuel Cells*, 2011, **11**, 26–37.
- 217 S. L. Lin and J. N. Bardsley, *Comput. Phys. Commun.*, 1978, **15**, 161–163.
- 218 W. Visscher, *Phys. Rev. A: At., Mol., Opt. Phys.*, 1974, **10**, 2461–2472.
- 219 G. E. Murch and R. J. Thorn, *Philos. Mag.*, 1977, **36**, 529–539.
- 220 G. Murch, *Solid State Ionics*, 1982, **7**, 177–198.
- 221 D. Y. Wang and A. S. Nowick, *J. Solid State Chem.*, 1980, **35**, 325–333.
- 222 J. Koettgen and M. Martin, in preparation.
- 223 Jülich Supercomputing Centre, *J. Large-Scale Res. Facil.*, 2016, **2**, A62.
- 224 M. Ismail, E. Ahmed, A. M. Rana, I. Talib and M. Y. Nadeem, *J. Alloys Compd.*, 2015, **646**, 662–668.